

In-depth analysis of reactive bubbly flow using two-way coupled spatio-temporal 1D model

Vincent Ngu, Jérôme Morchain, Arnaud Cockx*

TBI, Université de Toulouse, CNRS, INRAE, INSA, Toulouse, France

HIGHLIGHTS

- Two-way coupled 1D model successfully implemented for CO₂ reactive absorption.
- 1D model yields excellent agreement with experimental and literature data.
- Asymptotic model unravels the governing parameters at each pH zone.
- Sensitivity analyses show the importance of k_L in capturing the transient process.

ARTICLE INFO

Article history:

Received 8 April 2022

Received in revised form 24 June 2022

Accepted 29 July 2022

Available online 3 August 2022

Keywords:

Bubble column

Gas-liquid multiphase flow

Mass transfer

CO₂ absorption

Chemical reaction

1D modeling

ABSTRACT

This work aims to investigate reactive bubbly flow using a comprehensive spatio-temporal 1D model. The work of Darmana et al. (2007) who conducted experimental and numerical study on CO₂ chemisorption in NaOH solution is used as the reference case. The gas-liquid hydrodynamics are well captured using a drift-flux loop model. During the transient process, bubble diameter d_b shrinkage from 5.5 mm at the inlet to 3.7 mm at the outlet is captured by the 1D model. The pH evolution is also well predicted by the 1D model provided that appropriate closures are applied, including the recently proposed enhancement factor and reaction pathway by Krauß & Rzehak (2017). An asymptotic 0D model is proposed to highlight the key parameters involved during the transient chemisorption process which are enhancement factor E , mass transfer coefficient k_L , and interfacial area a . Sensitivity analyses on liquid axial dispersion coefficient, enhancement factor and mass transfer coefficient are then performed to elucidate their impact on reactive mass transfer. As the process is controlled by interfacial mass transfer, the most important parameters are k_L and d_b description.

© 2022 Elsevier Ltd. All rights reserved.

1. Introduction

Bubble column reactors are commonly used in the industry, such as metallurgical, petrochemical, biochemical, and water treatment. These reactors have numerous advantages: (a) simple design, (b) absence of mechanical stirring device (c) good mixing (d) low energy input requirements and (e) large gas-liquid contact area (Deckwer and Schumpe, 1993; Kantarci et al., 2005; Shah et al., 1982). However, complex and highly coupled phenomena in terms of multiphase flow, mass and heat transfer, and (bio) reaction prevail in such system.

In reactive bubble column, the hydrodynamics, mass transfer, and reactions are highly coupled with each other. The reaction rate depends on the local availability of the species, which is controlled

by the convection, the mixing of the fluid flow, and the gas-liquid mass transfer (if the species is originated from the gaseous phase). The interphase mass transfer flux is driven by the species concentration gradient diffused between phases, which depends on the mass transfer coefficient and interfacial area (hence the local bubble size and gas holdup). Besides, the mass transfer coefficient is a function of the bubble size and local hydrodynamics, which are also affected by the overall gas-liquid reaction rate. In short, the coordinated and mutual influence of these complex processes make the overall reactor performance prediction and scale-up of reactive bubble column very challenging (Buffo et al., 2017; Darmana et al., 2007). Fig. 1a depicts the coupling of these phenomena through different physical parameters involved in reactive bubbly flow.

Recently, extensive efforts have been made to develop numerical code to simulate bubble column reactor (Hlawitschka et al., 2017; McClure et al., 2014; Rzehak et al., 2017; Rzehak and Krepper, 2016). Most of the works have been performed using

* Corresponding author.

E-mail addresses: ngu@insa-toulouse.fr (V. Ngu), morchain@insa-toulouse.fr (J. Morchain), cockx@insa-toulouse.fr (A. Cockx).

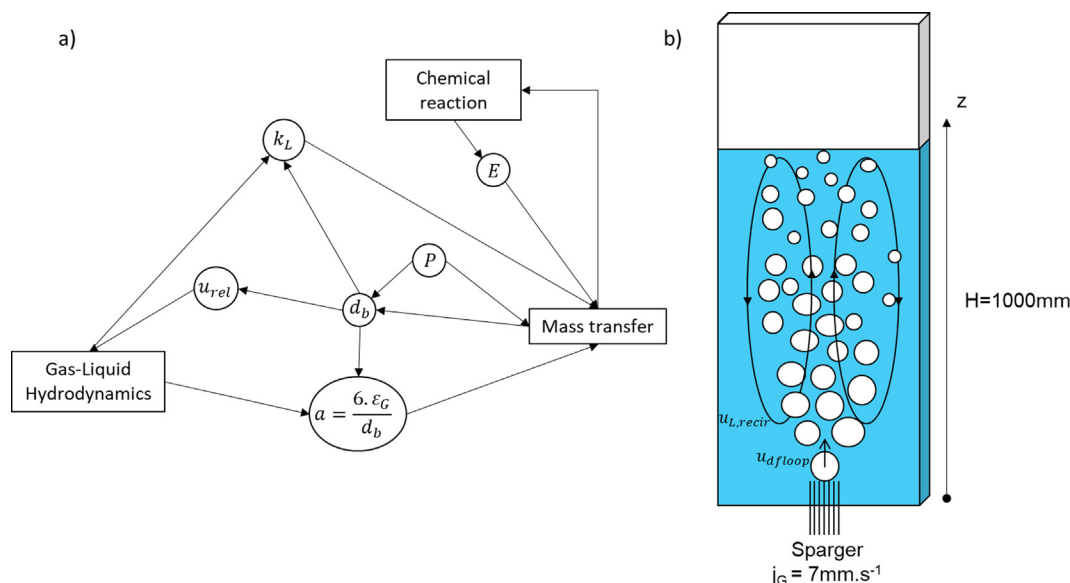


Fig. 1. (a) Interdependency diagram of hydrodynamics, mass transfer and chemical reaction through different parameters involved in reactive bubbly flow. (b) Simplified sketch of the pseudo-2D bubble column studied by Darmana et al. (2007).

Computational Fluid Dynamics (CFD) approach as it is a powerful tool to capture the spatial heterogeneities and to study the local interaction of multiphase systems. In general, two approaches are used in the CFD framework, i.e., Euler-Euler and Euler-Lagrange simulations. Apart certain studies on industrial-scale bubble column (Cockx et al., 1999; Ertekin et al., 2021; Rehman et al., 2017), most of the numerical work focus on lab-scale bubble column. Krauß and Rzehak (2018) pointed out that most of the numerical work focus on the fluid dynamics of bubbly flows. The mass transfer modeling, particularly with the reactive flow is less common in the literature. The presence of reactive system coupled with mass transfer phenomenon, makes the mass transfer modeling highly challenging. Extensive studies are needed to unravel the influence of reactive mass transfer on the hydrodynamics behavior. Moreover, progress in simulation studies is hindered by a shortage of high-quality validation data. This is mostly due to the difficulty to access local value such as concentration measurements (Krauß and Rzehak, 2018; Rzehak and Krepper, 2016). Lately, Chen and Brooks (2021) conducted a comprehensive experiment on local mass transfer in small-scale bubble column (5-inch diameter and 6.55-inch height) and the CFD model developed by the authors is validated in terms of hydrodynamics and mass transfer. A detailed study with local concentration measurements at a larger-scale bubble column was carried out by Deckwer et al. (1978) and their data was later used in the work of Rzehak and Krepper (2016) whereby Euler-Euler CFD simulation was performed. Rzehak and Krepper (2016) concluded that new measurements will be needed as spatially resolved data which are suitable for CFD model validation is still scarce in the literature.

In the reference work of Darmana et al. (2007), the chemisorption of carbon dioxide (CO_2) in aqueous sodium hydroxide solution (NaOH) was investigated and the influence of fast reaction on the hydrodynamics behavior was studied both experimentally and numerically with the CFD model using Euler-Lagrange approach. In the past, several numerical attempts have been conducted to compare with Darmana's work. As demonstrated in several literature findings, reactive absorption of CO_2 in NaOH is a fast and highly coupled reaction as the shrinkage of bubble size is observed which in returns affects the CO_2 mass transfer flux and the reaction rate (Buffo et al., 2017; Darmana et al., 2007; Gruber et al., 2015). Most of the studies on Darmana et al. (2007) reference case have

been performed using CFD framework, either in Euler-Euler (Hlawitschka et al., 2016; Krauß and Rzehak, 2018; Liu et al., 2021) or Euler-Lagrange (Gruber et al., 2015; Huang et al., 2021; Taborda and Sommerfeld, 2021) approach. These studies applied different strategies separately to investigate or reproduce the experimental data, such as detailed reaction pathways (Krauß and Rzehak, 2018; Krauß and Rzehak, 2017), bubble population model (Buffo et al., 2017; Gruber et al., 2015), mass transfer closure model (Huang et al., 2021; Taborda and Sommerfeld, 2021), and enhancement factor model (Huang et al., 2021; Krauß and Rzehak, 2017).

To our best knowledge, no studies have been done using one-dimensional (1D) modeling approach for this reference case. The 1D model requires less computational resources than sophisticated CFD model and it is easy to implement, hence it offers a fast and satisfactory prediction (Siebler et al., 2020). Although there is some trade-off in terms of highly precise spatial resolution offered by the CFD model, the 1D model is still very useful for probing and filtering off a wide range of design and operating parameters or closure models before moving into advanced CFD modeling which aims at studying the local field structure and the interactions between phases. The 1D model is commonly used to model bubble columns in the literature as it provides satisfactory performance prediction at low computational costs (Camarasa et al., 2001; Colombet et al., 2013; Hissanaga et al., 2020; Larsson et al., 2022; Talvy et al., 2007). However, most of the model make some assumptions such as constant gas holdup and constant bubble diameter. These assumptions cannot be made in the case of Darmana et al. (2007), as the bubble diameter changes considerably in the axial direction due to reactive absorption.

A two-way coupled and spatio-temporal approach have to be considered in the case of fast reaction. This paper aims to demonstrate that a full 1D two-way coupled spatio-temporal model is able to reproduce Darmana's results without performing computational-intensive calculations. The goal is to decipher and characterize the hydrodynamics-reactive mass transfer coupling process. Following the literature results, similar conclusions and some new insights are also drawn using the 1D model. This paper is organized as follows. A summary of the reference work of Darmana et al. (2007) is briefly recalled in Section 2.1. Next, the 1D model and the closure models applied are described in

Section 2.2. A comparison to some literature data is presented in [Section 3](#). An asymptotic model based on CSTR assumption is also proposed in [Section 4](#) to better understand the underlying physical mechanism that impact the temporal pH evolution. Besides, it helps to identify essential parameters which play an important role at different time zone in describing the CO₂ chemisorption process. Lastly, sensitivity analysis that highlights important parameters of reactive bubbly flow is presented in [Section 5](#). [Section 6](#) summarizes our findings and final remarks.

2. Materials & methods

2.1. Brief summary of Darmana's case

Full description of the methods and the results can be found in the original work of [Darmana et al. \(2007\)](#). For the sake of simplicity, a brief recap of the work is reported here. A simplified sketch of the bubble column used is shown in [Fig. 1b](#).

The experimental setup consisted of a lab-scale pseudo-2D bubble column of 200 mm width and 30 mm depth. The initial liquid level (H) was kept at 1000 mm. The gas was sparged through 21 needles arranged with a square pitch of 5 mm and it was located at the column center. The superficial gas velocity (j_G) was kept as 7 mm.s⁻¹. The bubble size formed at the inlet (d_{b0}) was mentioned to be 5.5 mm.

Two gas–liquid systems were measured to investigate the influence of fast reaction on the hydrodynamics behavior. First, nitrogen (N₂) and twice distilled water was used to mimic the non-reactive system. Next, a reactive system composed of CO₂ and aqueous NaOH solution at an initial pH of 12.5 was utilized to study the effect of chemisorption on the hydrodynamics. Several measurements were conducted, namely:

- Integral gas holdup was calculated by the difference of liquid height with and without bubbles.
- Time-averaged gas velocity was measured by using Particle Image Velocimetry (PIV) as a tracking method of the bubble. The bubble velocity profile was reported at $z/H = 0.75$.
- Local bubble size measurements were obtained through image processing technique of a series of images recorded via CCD camera. The time-averaged bubble size axial profile was reported only for reactive case.
- Temporal evolution of pH was measured with a pH probe placed at 2 cm below the liquid surface in the center of the column.

Besides the experimental work, [Darmana et al. \(2007\)](#) also carried out numerical simulations for both non-reactive and reactive cases using the CFD Euler-Lagrange approach. The motion of each individual bubble is computed from the bubble mass and momentum equations while considering all relevant fluid dynamical forces, namely gravity, buoyancy, drag, lift, virtual mass and wall forces. The drag, lift and wall forces are modeled using closures obtained from [Tomiyama et al. \(2002, 1995\)](#).

2.2. Comprehensive 1D spatio-temporal model for reactive bubbly flow

2.2.1. Two-phase hydrodynamics model

Previously developed comprehensive two-way coupled 1D model is used in this work and it is recalled here. The numerical discretization and the applied scheme are kept the same as that described in [Ngu et al. \(2022\)](#). The 1D model is composed of the following species transport equations, and they are solved for 4 species $i \in \{CO_2; OH^-; HCO_3^-; CO_3^{2-}\}$:

Gas:

$$\frac{\partial \varepsilon_G C_{G,i}}{\partial t} + \frac{\partial u_G \varepsilon_G C_{G,i}}{\partial z} = D_G \frac{\partial}{\partial z} \left(\varepsilon_G \frac{\partial C_{G,i}}{\partial z} \right) - Ek_{L,i} a (C_i^* - C_{L,i}) \quad (1)$$

Liquid:

$$\frac{\partial \varepsilon_L C_{L,i}}{\partial t} + \frac{\partial u_L \varepsilon_L C_{L,i}}{\partial z} = D_L \frac{\partial}{\partial z} \left(\varepsilon_L \frac{\partial C_{L,i}}{\partial z} \right) + Ek_{L,i} a (C_i^* - C_{L,i}) + \varepsilon_L R_i \quad (2)$$

$$\varepsilon_G + \varepsilon_L = 1 \quad (3)$$

Equation (1) is solved only for CO₂, whereas equation (2) is solved for CO₂, OH⁻, HCO₃⁻, CO₃²⁻. Apart from CO₂, the mass transfer term ($Ek_{L,i} a (C_i^* - C_{L,i})$) is zero. ε_G and ε_L are the gas and liquid holdup summing as unity as shown in equation (3). $C_{G,i}$ and $C_{L,i}$ are the concentration of species i , which will also be represented with $[i]$ in this work, e.g. [CO₂] concentration of CO₂.

The gas phase hydrodynamics is modeled via a drift-flux loop model (u_{dfloop}) which is derived hereafter. The relative gas velocity of the mixture (u_{rel}) can be derived from a momentum balance on an isolated bubble having reached its terminal velocity, expressed as:

$$u_{rel} = \sqrt{\frac{4 g (\rho_m - \rho_G) d_b}{3 \rho_L C_D}} \quad (4)$$

With g the gravity (9.81 m.s⁻²), ρ_m and ρ_G the mixture and gas density, respectively; d_b is the bubble diameter and C_D is the drag coefficient. The mixture density ρ_m is calculated as $(\rho_L \varepsilon_L + \rho_G \varepsilon_G) - \rho_G = \varepsilon_L (\rho_L - \rho_G)$. The density of water (1000 kg.m⁻³) and carbon dioxide (1.78 kg.m⁻³) at 298.15 K and 1 atm are taken for liquid and gas density, respectively. The drag coefficient proposed by [Tomiyama et al. \(1998\)](#) for pure system is used, similar to [Darmana et al. \(2007\)](#). It is written as:

$$C_D = \max \left\{ \min \left[\frac{16}{Re} (1 + 0.15 Re^{0.687}), \frac{48}{Re} \right], \frac{8}{3} \frac{Eo}{(4 + Eo)} \right\}$$

$$Re = \frac{u_{rel} d_b}{\nu_L} \quad Eo = \frac{(\rho_L - \rho_G) g d_b^2}{\sigma} \quad (5)$$

With Re the Reynolds and Eo the Eötvös number. The viscosity and surface tension of water is applied ($\mu_L = 10^{-3}$ Pa.s and $\sigma = 0.072$ N.m⁻¹). The variations of Re and Eo are between 800 and 1600 and 1.4 – 4.2, respectively for both non-reactive and reactive cases. In this range of Re and Eo , the drag coefficient is governed by the Eötvös term, signifying that the governing factor is no longer the viscous force but the pressure and surface tension forces ([Tomiyama et al., 1998](#)). No collective effect is included as the gas holdup shown in [Darmana et al. \(2007\)](#) is relatively low (lower than 3%). The axial bubble velocity profile obtained by [Darmana et al. \(2007\)](#) is parabolic, showing the non-uniformity of the flow, due to the centered gas inlet. Considering this non-uniformity bubbly flow, the drift-flux model (u_{df}) suggested by [Zuber and Findlay \(1965\)](#), which is commonly used in 1D modeling is applied here ([Camarasa et al., 2001; Talvy et al., 2007](#)). It stated that the gas velocity is composed of two components: (i) gas transport induced by the mixture velocity $\langle j \rangle$, which is the sum of gas and liquid superficial velocity ($j = j_G + j_L$) and (ii) the buoyancy driven gas transport u_{rel} . The drift-flux model is expressed as:

$$u_{df} = C_0 \langle j \rangle + u_{rel} \quad (6)$$

Here, the coefficient C_0 is calculated from its definition $C_0 = \frac{\langle \varepsilon_G j \rangle}{\langle \varepsilon_G \rangle \langle j \rangle}$ using [Darmana et al. \(2007\)](#) reported profiles, and a value of 1.24 and 1.27 are obtained for non-reactive and reactive case, respectively.

The experimental liquid axial velocity profile obtained by Darmana et al. (2007) suggests that the bubbles rise in the column center with liquid recirculation down near the wall. This liquid recirculation phenomena leads to the hydrodynamic of the column to behave like an airlift system (Talvy et al., 2007, 2005). Thus, the liquid recirculation velocity $u_{L,recirc}$ is considered as j_L in the drift-flux model in equation (6), leading to drift-flux loop u_{dloop} model, written as.

$$u_{dloop} = C_0(j_G + u_{L,recirc}) + u_{rel} \quad (7)$$

The value of $u_{L,recirc}$ is also derived from the liquid axial velocity profile from Darmana et al. (2007) through spatial averaging till the inversion point of liquid velocity – point where the liquid flow direction changes to downward flow. This mean value of $u_{L,recirc}$ varies with or without reaction due to the gas holdup changes and they are given in Table 2. In the end, the gas velocity u_G is calculated with the drift-flux loop model u_{dloop} expressed in equation (7).

The liquid side axial dispersion coefficient (D_L) is taken from the correlation of Deckwer et al. (1974) while the gaseous side axial dispersion coefficient (D_G) is estimated with the correlation of Wachi and Nojima (1990). The bubble column diameter (D_r) is taken as the equivalent diameter of a circular bubble column having the same cross sectional area as that of a rectangular column, similar to the work of Alexander and Shah (1976), which yields $D_r = 0.087$ m. These coefficients are expressed in equations (8) and (9). The correlations yield a value of $5 \times 10^{-3} \text{ m}^2 \cdot \text{s}^{-1}$ and $3.6 \times 10^{-3} \text{ m}^2 \cdot \text{s}^{-1}$ for D_L and D_G , respectively. D_L can be breakdown into several terms to assess the contribution of each dispersion phenomena (Talvy et al., 2007). The CO_2 molecular diffusivity in water is in the order of $10^{-9} \text{ m}^2 \cdot \text{s}^{-1}$, the turbulent diffusivity can be considered as the turbulent viscosity ν_t , which can be estimated using Chou model, given as $\nu_t = U^* \kappa \delta$ with $\kappa = 0.4$ (Chou, 1945; Launder and Spalding, 1974). The length scale δ is taken as the half depth of the column (15 mm), U^* can be supposed as 5% of averaged bubble velocity initially estimated as $0.3 \text{ m} \cdot \text{s}^{-1}$. Therefore, the turbulent velocity is estimated as $\nu_t = 0.05 \cdot 0.3 \cdot 0.4 \cdot 0.015 \approx 10^{-4} \text{ m}^2 \cdot \text{s}^{-1}$. Thus, the main contribution of axial dispersion in the liquid phase is the spatial dispersion as in Talvy et al. (2007).

$$D_L = 2 \cdot 7 \cdot 10^{-4} \cdot (D_r \cdot 100)^{1.4} \cdot (j_G \cdot 100)^{0.3} \quad (8)$$

$$D_G = 20 \cdot D_r^{1.5} \cdot j_G \quad (9)$$

Due to mass transfer, bubble shrinkage is expected. The changes in bubble diameter d_b is described by equation (10):

$$d_b = d_{b0} \sqrt[3]{\frac{\varepsilon_G}{\varepsilon_{G0}}} \quad (10)$$

The inlet bubble diameter (d_{b0}) are taken the same as Darmana et al. (2007) at 5.5 mm. The interfacial area (a) is calculated with bubble diameter and gas holdup, expressed as:

$$a = 6 \frac{\varepsilon_G}{d_b} \quad (11)$$

Table 1
Summary of reaction term for each species i .

Species i	$R_i (\text{kmol} \cdot \text{m}^{-3} \cdot \text{s}^{-1})$
CO_2	$-R_{1,1} + R_{1,2} - R_{3,1} + R_{3,2}$
OH^-	$-R_{1,1} + R_{1,2} - R_{2,1} + R_{2,2} - R_{3,1} + R_{3,2}$
HCO_3^-	$R_{1,1} - R_{1,2} - R_{2,1} + R_{2,2} + R_{3,1} - R_{3,2}$
CO_3^{2-}	$R_{2,1} - R_{2,2}$

Table 2

Input parameters applied in the 1D model for the reference case.

Input Parameters	Value	Units
d_{b0}	5.5	mm
T	298.15	K
j_G	0.007	$\text{m} \cdot \text{s}^{-1}$
pH ₀	12.5	–
C_0 without reaction	1.24	–
C_0 with reaction	1.27	–
$u_{L,recirc}$ without reaction	0.066	$\text{m} \cdot \text{s}^{-1}$
$u_{L,recirc}$ with reaction	0.042	$\text{m} \cdot \text{s}^{-1}$

The mass transfer closure model (k_L) is calculated from the Sherwood (Sh) correlation derived for non-spherical bubbles situated in the wobbling regime (Brauer, 1979). The expression is given in Table 3. The calculations of the solubility $C_{\text{CO}_2}^*$ and diffusivity D_{CO_2} are detailed in Appendix A and Appendix B, respectively.

2.2.2. Reactive model

The reaction term (R_i) calculation follows the recent work of Krauß and Rzehak (2018). The description of the reaction term R_i in the 1D model is briefly explained here. The dissolved CO_2 will react in a two-step reversible reaction which will be denoted as the first and second reactions in this work. The reactions are written as follows:



Where $k_{1,1}$ and $k_{1,2}$ are the forward and backward rate constants, respectively for the first reaction while $k_{2,1}$ and $k_{2,2}$ are the forward and backward rate constants for the second reaction.

The water reaction path becomes important at pH less than 10 and even dominant at pH less than 8 (Kern, 1960). It consists of two steps, the first of which, is written as:



The first step is reversible (Kern, 1960). The second step is identical to hydroxide path (equation (13)), with the two pathways coupled by the auto-dissociation of water associated with the equilibrium constant K_w .



Therefore, the corresponding chemical reactions rates for equations (12)–(14) are expressed as:

$$R_{1,1} = k_{1,1} \cdot [\text{CO}_2] \cdot [\text{OH}^-] \quad (16)$$

$$R_{1,2} = k_{1,2} \cdot [\text{HCO}_3^-] \quad (17)$$

$$R_{2,1} = k_{2,1} \cdot [\text{HCO}_3^-] \cdot [\text{OH}^-] \quad (18)$$

Table 3

Closure models applied in the 1D model for the reference case.

Parameters	Correlation
u_G	$u_G = u_{dloop} = C_0(j_G + u_{L,recirc}) + u_{rel}$
D_L	$D_L = 2.7 \cdot 10^{-4} \cdot (D_r \cdot 100)^{1.4} \cdot (j_G \cdot 100)^{0.3}$
D_G	$D_G = 20 \cdot j_G \cdot D_r^{1.5}$
k_L	$Sh = 2 + 0.015 Re^{0.89} Sc^{0.7} \quad Sh = \frac{k_L d_b}{D_{\text{CO}_2}}; Re = \frac{u_{rel} d_b}{\nu_t}; Sc = \frac{\nu_t}{D_{\text{CO}_2}}$
E	$E = -\frac{Ha^2}{2(E_i - 1)} + \sqrt{\frac{Ha^4}{4(E_i - 1)^2} + E_i \frac{Ha^2}{4(E_i - 1)} + 1}$ E_i from equations (B.4)–(B.6) of Krauß and Rzehak (2017)

$$R_{2,2} = k_{2,2} \cdot [\text{CO}_3^{2-}] \quad (19)$$

$$R_{3,1} = k_{3,1} \cdot [\text{CO}_2] \quad (20)$$

$$R_{3,2} = k_{3,2} \cdot [\text{HCO}_3^-] \cdot [\text{H}^+] = k_{3,2} \cdot [\text{HCO}_3^-] \cdot \frac{K_w}{[\text{OH}^-]} \quad (21)$$

Here, the reaction rate $R_{j,k}$ are expressed in $\text{kmol.m}^{-3}.\text{s}^{-1}$ with $j = 1, 2, 3$ denotes the reactions of equations (12)–(14) and $k = 1, 2$ denotes the forward and backward reactions, respectively. The calculation of the reaction rate constants $k_{j,k}$ are detailed in the Appendix C. The reaction term R_i for each species i in equation (2) is calculated with the expressions given in Table 1.

2.2.3. Enhancement factor model

Due to fast chemical reaction, enhancement of mass transfer flux has to be considered.

A simple enhancement factor model (E) has been proposed by Fleischer et al. (1996) which is obtained from the fitting to the experimental data. The model stated that if the OH^- mass fraction is higher than a certain threshold, E is activated. It is expressed as:

$$E = \begin{cases} 1, & Y_{\text{OH}^-} < 1.8e - 6 \\ 1241.3Y_{\text{OH}^-} + 1.0069, & Y_{\text{OH}^-} \geq 1.8e - 6 \end{cases} \quad (22)$$

This model has been used in many existing works (Hlawitschka et al., 2016; Huang et al., 2021; Liu et al., 2021), primarily due to its simplicity. Up to pH of 10, the enhancement factor is close to unity (Hlawitschka et al., 2016). It is pointed out by Huang et al. (2021) that this model gives the best fit to Darmana's experimental pH curve when the authors compared this correlation with other enhancement factor models.

Recently, Krauß and Rzehak (2017) proposed another enhancement factor model based on the fit formula of an instantaneous one-step second-order reaction. The model is briefly presented here, as the details can be found in the original paper. Here, a fast single-step irreversible second order reaction is considered by combining equation (12) and (13). This leads to the following overall reaction equation:



The Hatta number (Ha) is thus written as:

$$Ha = \frac{\sqrt{k_{1,1} \cdot D_{\text{CO}_2}} \cdot [\text{OH}^-]}{k_L} \quad (24)$$

With the renewal theory, an expression for the enhancement factor derived by DeCoursey (1974) is expressed as:

$$E = -\frac{Ha^2}{2(E_i - 1)} + \sqrt{\frac{Ha^4}{4(E_i - 1)^2} + E_i \frac{Ha^2}{4(E_i - 1)}} + 1 \quad (25)$$

With E_i is the instantaneous enhancement factor. E_i must be greater or equal to one to always give a value of E greater or equal to one. Otherwise, the value is limited by $\max(E, 1)$ (Westertep et al., 1998). To apply this model, an expression of E_i is needed. An implicit solution was given by Danckwerts and Lannus

(1970), however, it is difficult to resolve and thus, less practical for modeling purpose. Krauß and Rzehak (2017) proposed an explicit fit formula to overcome the complexity of the implicit model. The explicit E_i model is used in this work but it is not detailed here as it can be found in Appendix B of Krauß and Rzehak (2017).

The impact of E is investigated in this work and it will be discussed in Section 5.2. The results given by the E of Fleischer et al. (1996) and Krauß and Rzehak (2017) are compared. In the first step, the results presented hereafter used the latest development of E which is that of Krauß and Rzehak (2017) unless it is stated otherwise.

In short, the input parameters and the closure models used for the reference study are summarized in Table 2 and Table 3, respectively. Apart from the reference results of Darmana et al. (2007), some additional and more recent CFD results in the literature are also used in the comparison with the 1D model, as indicated with a "x" in Table 4. These results included transient gas holdup, local gas holdup, local bubble velocity, local bubble diameter, and temporal pH evolution. For non-reactive case, the reactive term is not solved to calculate the integral gas holdup. The integral gas holdup is calculated by spatial averaging gas holdup at $t_\infty = 250$ s. The initial concentrations of sodium and hydroxide ions were set to match the initial pH value of 12.5, while all other species were set to zero. For reactive case, the reactive term is activated and the initial hydrodynamics start from the converged non-reactive case. The model is spatially discretized for 50 node grids and it is solved using MATLAB 2017b stiff solver ode15s where the timestep is adaptative as explained in Ngu et al. (2022).

3. Results of 1D model compared with previous works

3.1. Hydrodynamics with and without CO_2 reactive absorption

In this section, the hydrodynamics results on the non-reactive and the reactive system are addressed. In most cases, Darmana et al. (2007) employed time-averaging for the interpretation of the dynamic results. It is reported that a time interval of 20–80 s and 20–95 s was used for the non-reactive and the reactive case, respectively. The same time interval for time-averaging is used in this work.

Table 5 presents the 1D time-averaged local bubble velocity compared with that of Buffo et al. (2017), Darmana et al. (2007), and Krauß and Rzehak (2018). In all work, the non-reactive case shows higher bubble velocity compared with the reactive case. In the reactive case, high CO_2 mass transfer flux leads to a reduction in bubble size, causing a decline in the bubble velocity as expected. This is further confirmed in Fig. 3a where the bubble size decreases considerably during CO_2 chemisorption. Table 6 depicts the 1D time-averaged local gas holdup compared with that of Darmana et al. (2007), Huang et al. (2021), and Krauß and Rzehak (2018). Again, the high CO_2 interfacial mass transfer flux leads to a significant reduction in the gas holdup. The global hydrodynamics is well captured by the 1D model as the bubble velocity and the gas holdup are at the same order of magnitude to the experimental data and the literature CFD results.

Table 4

List of references used for comparison with 1D model. E-L: Euler-Lagrange. E-E: Euler-Euler.

Reference	CFD approach	Transient gas holdup	Local gas holdup	Local bubble velocity	Local bubble diameter	pH
(Darmana et al., 2007)	E-L	–	x	x	x	x
(Buffo et al., 2017)	E-E	x	–	x	x	x
(Krauß and Rzehak, 2018)	E-E	x	x	x	x	x
(Huang et al., 2021)	E-L	–	x	–	–	x
(Hlawitschka et al., 2016)	E-E	–	–	–	–	x

Table 5Time-averaged bubble velocity in m.s^{-1} at $z/H = 0.75$ for non-reactive and reactive case. The experimental and CFD results are obtained by area-weighted average.

Case	Experiment	(Darmana et al., 2007) CFD	(Buffo et al., 2017) CFD	(Krauß and Rzehak, 2018) CFD	1D model
Non-reactive	0.21	0.20	0.25	0.25	0.31
Reactive	0.19	0.20	0.23	0.24	0.29

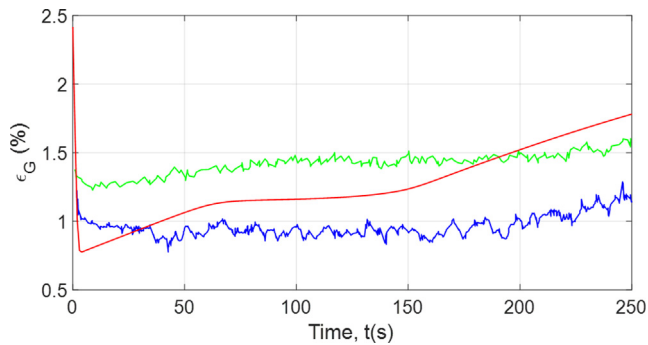
**Fig. 2.** Transient integral gas holdup during the CO_2 chemisorption. Red line from 1D model. Blue line from (Buffo et al., 2017) CFD results. Green line from (Krauß and Rzehak, 2018) CFD results.

Table 7 reports the integral gas holdup obtained by the 1D model and Darmana et al. data. The global hydrodynamics are correctly captured for both non-reactive and reactive cases as the integral gas holdup closely match that of experiment. The gas phase hydrodynamics play an important role in reactive bubbly flow. The bubbles hydrodynamic characterizes the gas holdup

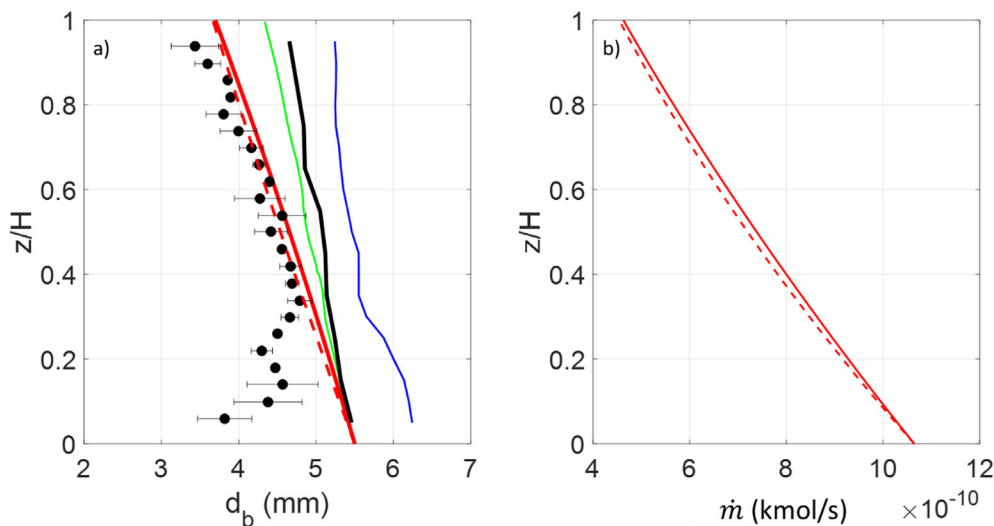
Table 7

Integral gas holdup in % from this work compared with experimental and simulation data of Darmana et al. (2007).

Case	Experiment	CFD Simulation	1D model
Non-reactive	2.3	2.2	2.42
Reactive	1.2	1.6	1.78

which characterizes the specific area a for mass transfer. Consequently, as long as the gas velocity is correctly described, the gas holdup, the mass transfer flux and the reaction rate should be correctly predicted.

Fig. 2 depicts the transient evolution of integral gas holdup in the column. The gas holdup drops immediately when the chemical reaction commences. It remains almost constant during the course of the chemisorption process. However, once the reaction is over, the gas holdup increases subsequently. Buffo et al. (2017) yields a lower integral gas holdup, mainly due to a larger initial bubble diameter (see Fig. 3), leading to a lower residence time. At the end of the neutralization process ($t = t_\infty$), the 1D model yields an integral gas holdup close to that of Krauß and Rzehak (2018). Two zones can be noticed for the transient gas holdup: (1) during the CO_2 chemisorption and (2) CO_2 physical absorption. During the chemical reaction process, the integral gas holdup remains almost

**Fig. 3.** (a) Time-averaged axial mean Sauter diameter profile. Blue line from (Buffo et al., 2017) CFD results, Green line from (Krauß and Rzehak, 2018) CFD results, Magenta lines from (Huang et al., 2021), Black line from (Darmana et al., 2007) CFD results, Black dots from (Darmana et al., 2007) experimental results, Red lines. – 1D model – equation (29) (b) Time-averaged local mass transfer rate of a single bubble predicted with $d_{b0} = 5.5$ mm. – Lagrangian model – equation (31).**Table 6**Time-averaged gas holdup in % at $z/H = 0.75$ for non-reactive and reactive case. CFD results are obtained by area-weighted average.

Case	(Darmana et al., 2007) CFD	(Huang et al., 2021) CFD	(Krauß and Rzehak, 2018) CFD	1D model
Non-reactive	2.09	2.99	3.05	2.38
Reactive	1.48	1.39	1.48	1.07

constant, which is translated by a steady CO₂ mass transfer flux (confirmed in Fig. 7) to the liquid. When the reaction is terminated, CO₂ starts to accumulate in the liquid, the dissolved CO₂ concentration increases. This results in an increasing gas holdup as the CO₂ mass transfer flux is diminishing, due to a weaker driving force (concentration gradient $C_{CO_2}^* - C_{L,CO_2}$). This phenomenon is also evidenced in the temporal gas holdup profile of Buffo et al. (2017), although they reveal a more modest increase.

The time-averaged axial bubble diameter profile during dynamic CO₂ chemisorption is presented in Fig. 3a. It shows that the bubble diameter shrinks due to high mass transfer flux when the bubbles rises in the column. 1D model yields relatively good bubble size reduction as the predicted bubble diameter is very close to the experimental measurements. Experimental measured bubble diameter was judged as unreliable up to a height of approximately 400 mm. In this region most of the bubbles overlaps and this could not be handled by the image processing algorithm, resulting in underestimated bubble size (Darmana et al., 2007). Nonetheless, most CFD models underpredict the bubble size shrinkage. Regardless, the bubble diameter has to be correctly quantified as it strongly impacts the mass transfer rate, and consequently the reaction rate. Fig. 3a shows that Buffo et al. (2017) model has the largest difference with the experimental data. This is due to the inlet bubble diameter applied by the authors is calculated from literature correlation which yields 6.2 mm and not 5.5 mm that is used by all other CFD works. If $d_{b0} = 5.5$ mm had been used in Buffo et al. (2017), the results could be better as the authors solved the bubble size population balance equation, which should yield a more realistic mass transfer flux. Darmana et al. (2007) underpredicts the bubble diameter shrinkage, mostly due to a lower mass transfer flux prediction. As shown in Fig. 3b the mass transfer rate of a single bubble ($\dot{m} = k_L \pi d_b^2 C_{CO_2}^*$) decreases with a factor of 2 between the top and the bottom of the column. This demonstrates that a slight error in terms of the bubble diameter prediction will generate larger errors in the transfer rate and subsequently the final pH value. The changes in mass transfer flux due to bubble diameter shrinkage can be explained with a simplified Lagrangian model of which it is detailed hereafter.

3.2. Role of bubble size on reactive mass transfer

By measuring the variation of bubble size with a video camera, it is able to evaluate experimentally the mass transfer coefficient, by knowing the mass transfer rate (Hori et al., 2017; Saito and Toriu, 2015; Takemura and Yabe, 1999; Tanaka et al., 2020). The same analogy can be applied here to relate the changes in bubble size due to the mass transfer rate, similar to the work of Solsvik (2018). The change in moles of CO₂ inside a bubble over time can be written as:

$$\frac{dn}{dt} = -k_L A_b (C_{CO_2}^* - C_{L,CO_2}) \quad (26)$$

With $A_b = \pi d_b^2$ the bubble surface area for mass transfer and n is the number of moles. Using the ideal gas law, $PV = nRT$ and assuming an isothermal process, equation (26) can be rewritten as:

$$\frac{\pi}{6RT} \frac{d(P \cdot d_b^3)}{dt} = -k_L A_b (C_{CO_2}^* - C_{L,CO_2}) \quad (27)$$

During 20–95 s of the reactive absorption, the dissolved CO₂ concentration is nearly zero (see Fig. 6b), C_{L,CO_2} can be considered equal to 0. If the column height and gas holdup are low, the pressure P can be supposed constant with an estimated value of

$\langle P \rangle = P_{atm} + \frac{\rho_L g H}{2} = 106230 \text{ Pa}$. The bubble velocity u_G for the range of d_b during the reactive absorption experiences little changes, leading to $dt = \frac{dz}{u_G}$. Equation (27) is rearranged to.

$$\frac{d(d_b^3)}{d_b^2} = -\frac{k_L C_{CO_2}^* 6RT}{u_G \langle P \rangle} \cdot dz \quad (28)$$

Assuming a constant u_G and k_L , integration of equation (28) leads to axial evolution of d_b expressed as.

$$d_b = d_{b0} \left(1 - \frac{k_L}{d_{b0}} \frac{z}{u_G} \frac{C_{CO_2}^* 2RT}{\langle P \rangle} \right) \quad (29)$$

Equation (29) reveals the term $\frac{k_L}{d_{b0}} \frac{z}{u_G}$ which can be interpreted as the ratio of the convection characteristic time ($\frac{z}{u_G}$) to the mass transfer characteristic time ($\frac{k_L}{d_{b0}}$). The lower the u_G , the higher the gas residence time, the higher the mass transfer flux, the smaller the bubble size due to mass transfer. Similarly, the higher the k_L , the higher the mass transfer flux, the higher the bubble shrinkage.

From equation (29), the axial evolution of mass transfer rate (\dot{m}) can be calculated as the evolution of $\frac{\dot{m}}{\dot{m}_0}$ is related to $\left(\frac{d_b}{d_{b0}}\right)^2$, leading to.

$$\frac{\dot{m}}{\dot{m}_0} = \left(1 - \frac{k_L}{d_{b0}} \frac{z}{u_G} \frac{C_{CO_2}^* 2RT}{\langle P \rangle} \right)^2 \quad (30)$$

By developing equation (30), it results in equation (31).

$$\dot{m} = \dot{m}_0 \left(1 - 2 \frac{k_L}{d_{b0}} \frac{z}{u_G} \frac{C_{CO_2}^* 2RT}{P} + \left(\frac{k_L}{d_{b0}} \frac{z}{u_G} \frac{C_{CO_2}^* 2RT}{P} \right)^2 \right) \quad (31)$$

With $\left(\frac{k_L}{d_{b0}} \frac{z}{u_G} \frac{C_{CO_2}^* 2RT}{P} \right)^2 \ll 2 \cdot \frac{k_L}{d_{b0}} \frac{z}{u_G} \frac{C_{CO_2}^* 2RT}{P}$, which is verified (results not shown) equation (31) can be simplified to.

$$\dot{m} = \dot{m}_0 \left(1 - 2 \frac{k_L}{d_{b0}} \frac{z}{u_G} \frac{C_{CO_2}^* 2RT}{P} \right) \quad (32)$$

Comparing equation (29) to equation (32), the reduction of \dot{m} is twice of that of d_b , meaning that any changes in d_b will lead to a two times modification in \dot{m} . The simplified expressions of axial evolution of d_b and \dot{m} are plotted together with that given by 1D model in Fig. 3. It is shown that the simplified Lagrangian model predicts the axial evolution of d_b and \dot{m} just as well as the 1D model. This is due to a small-scale column ($H = 1$ m), with relatively low-pressure effect, low gas holdup and no large changes in the bubble terminal velocity (bubble terminal velocity at 5.5 mm diameter nearly equals that at 4 mm diameter (Clift et al., 1978)).

The importance of the bubble diameter has already been highlighted in Buffo et al. (2017) and Liu et al. (2021). Indeed, the correct characterization of bubble diameter is crucial in the prediction of interfacial area (and thus the mass transfer flux) for such a highly-coupled fast reaction, as shown in Fig. 3.

Fig. 4a shows the significant pH evolution with different inlet bubble diameter. The results show the same conclusion as Buffo et al. (2017) (see Fig. 10 of Buffo et al. (2017)). A smaller bubble size creates higher specific gas–liquid contact area, resulting in a higher mass transfer flux. An inlet diameter of 4.5 mm overpredicts the mass transfer flux, hence, a faster drop in pH. The optimal inlet bubble diameter corresponds to the bubble diameter given by Darmana et al. (2007) – 5.5 mm. Inlet bubble diameter has a strong impact on the dynamic pH evolution ever since the beginning of the chemisorption process, as the CO₂ transfer flux has a direct influence on the OH[−] conversion rate. Notice that this mean Sauter diameter of 5.5 mm could represent reasonably the polydisperse

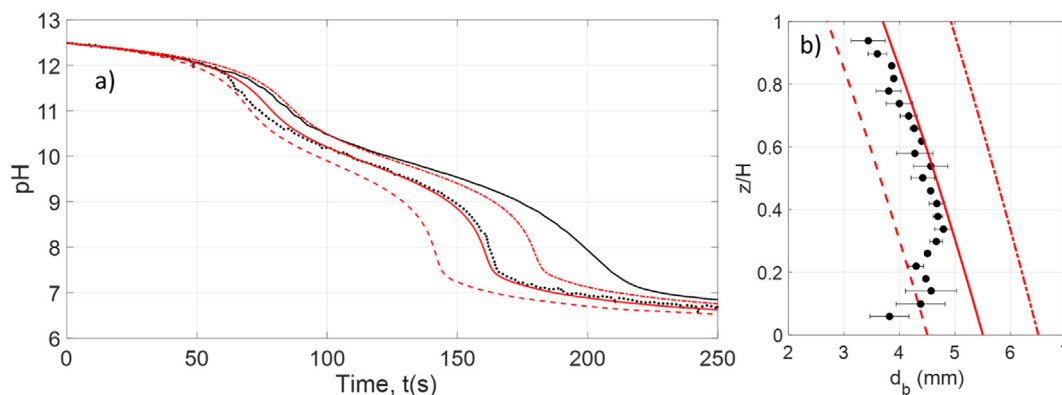


Fig. 4. (a) Time-dependent pH profile for 3 different inlet bubble diameters (d_{b0}). (b) Axial mean Sauter diameter profile. Black lines from (Darmana et al., 2007) CFD results, Black dots from (Darmana et al., 2007) experimental results, Red lines from 1D model. – $d_{b0} = 5.5$ mm, – $d_{b0} = 4.5$ mm, – $d_{b0} = 6.5$ mm.

bubble population between 4.5 and 6.5 mm without any consequence on the average mass transfer rate (equation (32)) if no coalescence or breakage occurs in the homogeneous bubbly flow regime, as supposed by the 1D model. In the industry, inlet bubble diameter has a strong impact on the bubble column mass transfer and reaction conversion efficiencies. Thus, the sparger design becomes an important issue as it determines the bubble size distribution at the inlet, which consequently characterizes the bubble diameter in the developed region. (Camarasa et al., 1999; McClure et al., 2016; Schäfer et al., 2002; Tirunehe and Norddahl, 2016). In Fig. 4b, the axial variation of bubble size is compared with inlet bubble size d_{b0} between 4.5 mm and 6.5 mm. It shows that $d_{b0} = 5.5$ mm seems to be the best fit.

Although the bubble formed at the inlet is mentioned to be 5.5 mm, no further explanation is given in Darmana et al. (2007) on how this bubble diameter is calculated as the measurement at this zone is judged to be unreliable experimentally. Here, it is attempted to understand the proposed 5.5 mm. With the orifice diameter $d_{or} = 1$ mm, CO_2 gas viscosity μ_G of $1.49 \times 10^{-5} \text{ m}^2 \cdot \text{s}^{-1}$ and the gas velocity at the orifice $U_{or} = 2.5 \text{ m} \cdot \text{s}^{-1}$ (supposing the gas flowrate is equally distributed in each orifice), the bubble Reynolds number at the orifice can be calculated using equation (33).

$$Re_{or} = \frac{\rho_G U_{or} d_{or}}{\mu_G} \quad (33)$$

One gets Re_{or} equals to 300 which suggests that the bubble formation is in the dynamic regime (McCann and Prince, 1971). Thus, the bubble diameter formed can be calculated with (Gaddis and Vogelpohl, 1986) model, written as.

$$\frac{d_{b0}}{d_{or}} = 1.16 \left(\frac{U_{or}^2}{d_{or} g} \right)^{\frac{1}{5}} \quad (34)$$

Equation (34) yields an initial bubble size of 4.3 mm. Considering the size of the sparger pitch of 5 mm, bubble coalescence can occur, resulting in larger bubble diameter at formation, which explain the higher d_{b0} of 5.5 mm. It is believed that the initial bubble diameter comes from the extrapolation of bubble diameter profile from the zone whereby the measurement is reliable. This inlet information is necessary as an input to subsequent numerical simulation. Hence, $d_{b0} = 5.5$ mm will be used for the rest of this work.

3.3. Importance of reaction pathway

The importance of correct reaction pathway has been demonstrated in the study of Krauß and Rzehak (2017) and Krauß and Rzehak (2018).

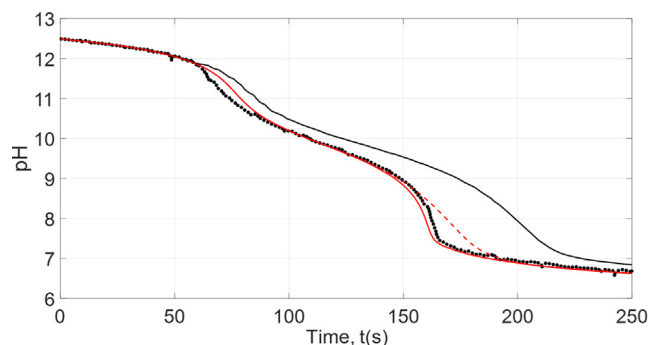


Fig. 5. Time-dependent pH profile using 2 or 3 reaction pathways. Black line from (Darmana et al., 2007) CFD results, Black dots from (Darmana et al., 2007) experimental results, Red lines from 1D model. – 3 reaction pathways, – 2 reaction pathways.

Fig. 5 shows that including the water pathway is essential to reproduce the experimental data. At the initial stage ($\text{pH} > 9$), the two curves overlap with each other, as all other parameters were taken the same and the third reaction is not activated. When the pH is less than 9, roughly when the time instant is in the range of 130–170 s, the water pathway becomes more and more dominant, as the third reaction rate becomes higher, as confirmed in Fig. 7. At the same time, the first reaction rate is getting smaller. If the water pathway is neglected, the total CO_2 consumption is only the first reaction rate, thus a weaker decrease in pH. The final pH value for both reaction pathways at steady-state remains the same even though the reaction rates are different between $t = 150$ – 200 s. The final pH value depends solely on the equilibrium constant of the chemical reaction (Liu et al., 2021). The water pathway only impacts the results when pH less than 9. In short, 1D model is in agreement with previous CFD works of Huang et al. (2021) and Krauß and Rzehak (2018). The third reaction has to be considered to describe the second change of pH slope.

3.4. pH and chemical species concentration evolutions

Local concentration of chemical species was not measured experimentally in the work of Darmana et al. (2007). Nevertheless, the local pH value at the outlet was recorded dynamically with a pH probe. This dynamic pH evolution indicates the consumption of hydroxide ions by the dissolved CO_2 . Therefore, an accurate CO_2 interfacial mass transfer flux prediction is required to reproduce the experimental pH curve with time. Fig. 6a shows that the pH evolution of the 1D model is consistent with the experi-

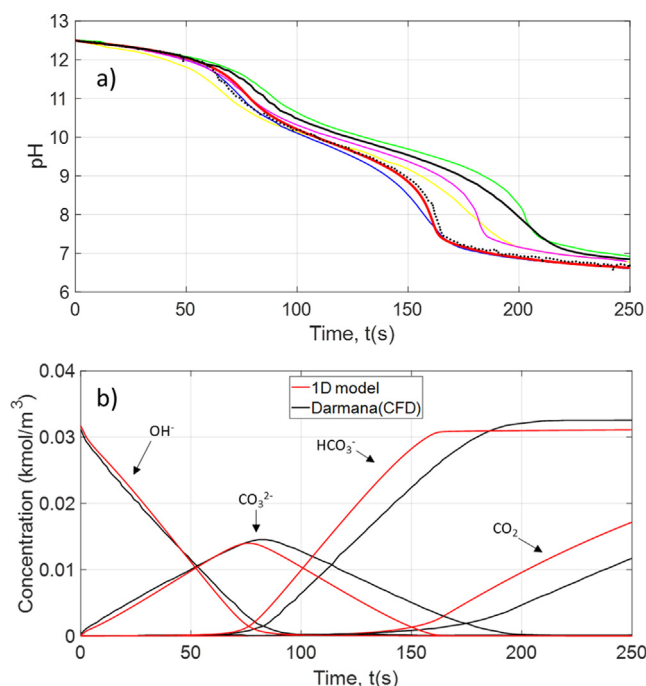


Fig. 6. (a) Time-dependent pH profile compared to existing literature results. Green line from (Krauß and Rzehak, 2018) CFD results, Magenta line from (Huang et al., 2021) CFD results, Blue line from (Buffo et al., 2017) CFD results, Yellow line from (Hlawitschka et al., 2016), Black lines from (Darmana et al., 2007) CFD results, Black dots from (Darmana et al., 2007) experimental results, Red lines from 1D model. (b) Temporal evolution of chemical species concentration.

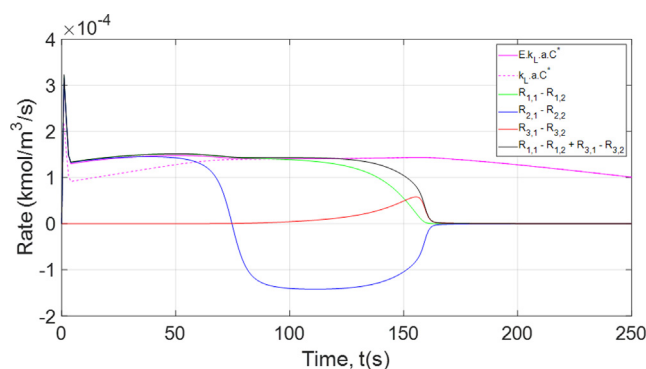


Fig. 7. Reaction rates and CO₂ mass transfer rate during the chemisorption process.

mental pH and other researchers work. The pH predicted by the 1D model also gives a better fit than Darmana's CFD model. The concentration temporal profile obviously has a slight difference than that of Darmana et al. (2007) CFD results, as reflected in the discrepancy of the two pH curves. In fact, the 1D model describes the pH evolution better than certain CFD model, mostly due to a better description of bubble size reduction – a key factor in determining the enhanced mass transfer flux (see Fig. 3a). By introducing an improved reaction pathway, as suggested by Krauß and Rzehak (2018), the second change in pH slope is also much better predicted. For example, for the case of Buffo et al., 2017, Darmana et al. (2007) and Hlawitschka et al., 2016, the second change in pH slope is not the same as that experimentally measured because the third pathway was not included in their model.

In Fig. 6b, it is interesting to observe that the final concentration of HCO₃⁻ corresponds to the initial concentration of OH⁻, indicating that conservation of mass is achieved in the whole reaction pro-

cess. This is also observed in all the work in the literature (Buffo et al., 2017; Hlawitschka et al., 2016; Huang et al., 2021; Krauß and Rzehak, 2018; Taborda and Sommerfeld, 2021), except in the original work of Darmana et al. (2007).

At the early stage of the reaction process, all the dissolved CO₂ reacts immediately with the hydroxide ions (OH⁻) and is converted into carbonate ions (CO₃²⁻). This is displayed in Fig. 6b with a decrease of [OH⁻] at the same time an increase in [CO₃²⁻], and in Fig. 7 whereby both $R_{1,1} - R_{1,2}$ and $R_{2,1} - R_{2,2}$ are positive, signifying the equations (12) and (13) are going in the forward reaction.

At approximately 75 s, [CO₃²⁻] reaches its maximum value and subsequently starts to decrease. This is reflected in Fig. 7 where $R_{2,1} - R_{2,2}$ turns negative, indicating that the equilibrium of the second reaction (equation (13)) starts to shift backward. Meanwhile, $R_{1,1} - R_{1,2}$ remains positive, meaning that the first reaction (equation (12)) is quasi irreversible. This results in an increase of bicarbonate (HCO₃⁻) concentration, as shown in Fig. 6b. With the consumption of both CO₃²⁻ and OH⁻, the pH continues to decrease. When the pH reaches 9, the third reaction commences, resulting in the formation of H⁺ ions, which triggers a steep change in the slope of pH curve. This corresponds to the moment when $R_{3,1} - R_{3,2}$ turns positive. At about 180 s, CO₃²⁻ is completely consumed and HCO₃⁻ reaches a steady concentration. The pH reaches a value of 7. In Fig. 7, it can be noticed that the CO₂ transfer rate equals to the reaction rate throughout most of the process until the start of CO₂ accumulation in the liquid at around 130 s.

After 180 s, the chemical reaction process ends as no more reactants (OH⁻) are present in the system. From this point onwards, the process switches to pure CO₂ physical absorption. Over time, the concentration of CO₂ increases meanwhile the CO₂ gas-liquid transfer rate decreases as the driving force decreases. The pH decreases gradually as the solution turns weakly acidic due to dissolved CO₂.

The CFD model provides more detailed local information on the reactive flow. Nevertheless, 1D model yields reliable axial evolution of the concentration, which is compared with the CFD work of Buffo et al. (2017). The results are shown in Fig. 8 whereby it reports the local concentration profiles of the dominant species at three different time instants ($t = 10$ s, 80 s and 200 s), as illustrated in Fig. 6b. At the early stage ($t = 10$ s), the pH is high as OH⁻ ions are the most abundant in the system. Dissolved CO₂ reacts immediately with OH⁻ and CO₃²⁻ is produced. At around 80 s, the CO₃²⁻ concentration peaks, and it acts as the dominant species. When the neutralization process reaches its late stage ($t = 200$ s), CO₂ accumulates in the liquid at a rate imposed by the physical absorption rate. Apart from the concentration of CO₂, all other species concentrations captured by 1D model are in the same order of magnitude with that of Buffo et al. (2017) CFD model. A slightly higher CO₂ concentration captured by the 1D model could likely due to the inlet bubble diameter d_{b0} applied is lower than that of Buffo et al. (2017) CFD model, as shown in Fig. 3a. At the final stage, the concentration of HCO₃⁻ reaches the initial concentration of OH⁻ (initial pH of 12.5 which is equivalent to 0.0316 kmol.m⁻³). All concentration profiles show a very weak spatial heterogeneity behavior as also depicted in the CFD results of Buffo et al. (2017). It shows that the temporal evolution is more important than the spatial heterogeneity due to the relatively well mixed liquid phase. Nevertheless, for the gas phase, a steadily decreasing $C_{CO_2}^*$ implies a decreasing mass transfer driving force and reaction rate along the axial direction.

In this section, it can be concluded that the two-phase hydrodynamics and the reactive pathway are validated by the 1D model. The 1D model agrees with the findings of the literature in terms

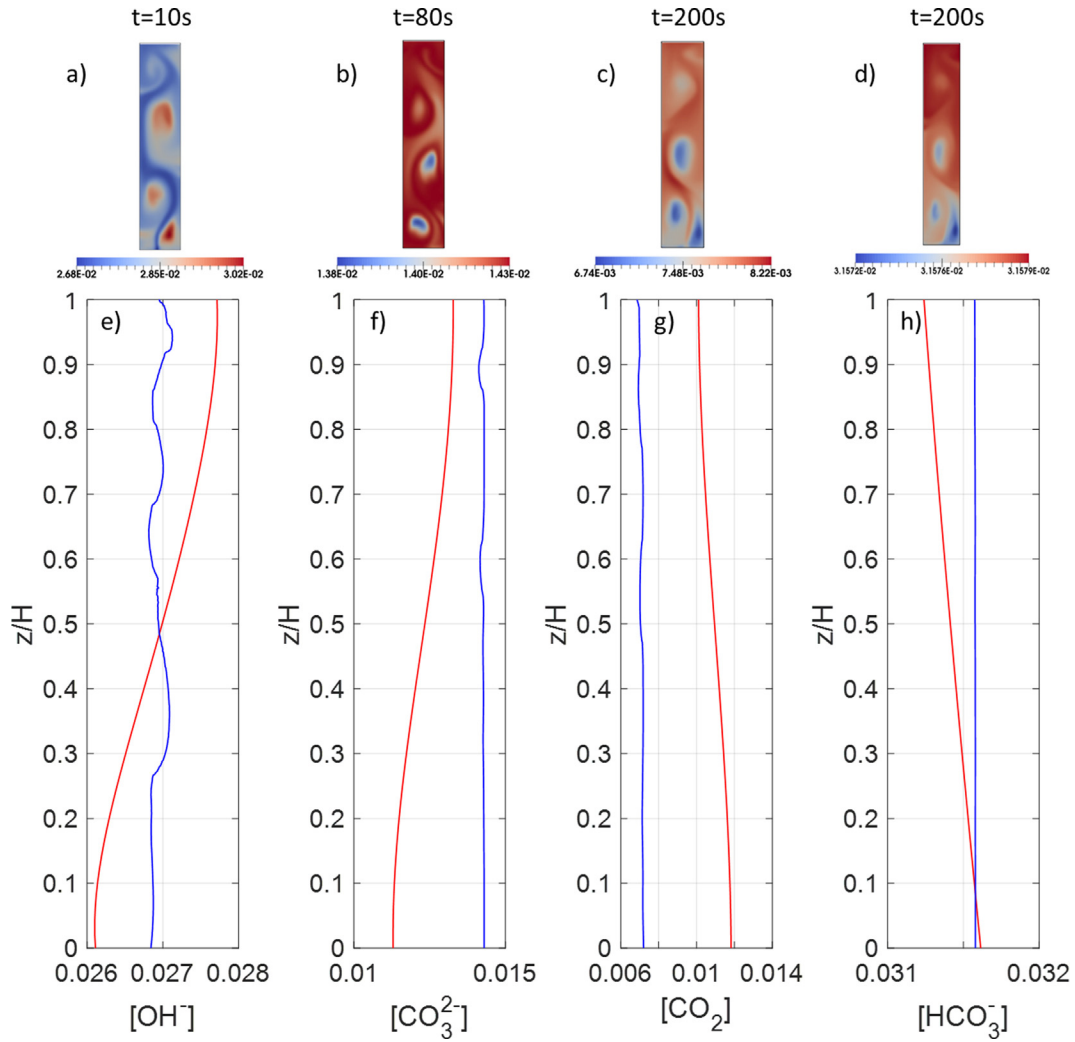


Fig. 8. Instantaneous spatial profiles of chemical species concentration at different instants. (a)–(d) CFD concentration contours are taken from Fig. 6 of (Buffo et al., 2017). (e)–(h) CFD results superposed with 1D results. Blue line from (Buffo et al., 2017) CFD results, Red lines from 1D model. CFD profiles are obtained through area-weighted average at each height.

of inlet bubble diameter (Buffo et al., 2017; Darmana et al., 2007; Liu et al., 2021) and the chemical kinetics model of Krauß and Rzehak (2017). Prior to sensitivity analyses, an asymptotic model is discussed to provide fundamental insights of reactive bubbly flow physics and to underline the main coupling phenomena occurring in each stage of the pH curve.

4. Asymptotic 0D model

In this section, an asymptotic model is derived to better understand the neutralization process. This asymptotic model helps to select the main parameters for the sensitivity analysis. Basic equations are presented here with the detailed development available in the *supplementary material*.

The asymptotic model is established in three phases and it only considered successive predominant species of each time interval, as shown in Fig. 6. In Phase 1, the chemical reactive species present in the system are OH^- and CO_3^{2-} . Meanwhile in Phase 2, the concentration of OH^- becomes negligible compared to other species and it is considered equals to zero. The transferred CO_2 forms HCO_3^- , hence $[CO_2]$ is still zero. Lastly in Phase 3, $[OH^-]$ and $[CO_3^{2-}]$ remains zero and only dissolved $[CO_2]$ changes at this period. Therefore, the

asymptotic model established for the three phases, after development, is given by the following equations:

Phase 1 ($t \in [0; t_1]$)

$$[OH^-] = [OH^-]_0 - 2.E.k_L.a.C_{CO_2}^*.t \quad (35)$$

$$[CO_3^{2-}] = E.k_L.a.C_{CO_2}^*.t \quad (36)$$

$$t_1 = \frac{[OH^-]_0}{2.E.k_L.a.C_{CO_2}^*} \quad (37)$$

Phase 2 ($t \in [t_1; t_1 + t_2]$)

$$[HCO_3^-] = 2.k_L.a.C_{CO_2}^*. (t - t_1) \quad (38)$$

$$[CO_3^{2-}] = [CO_3^{2-}]_{t_1} - k_L.a.C_{CO_2}^*. (t - t_1) \quad (39)$$

$$t_2 = \frac{[OH^-]_0}{2.k_L.a.C_{CO_2}^*} \quad (40)$$

Phase 3 ($t \in [t_1 + t_2; t_\infty]$).

$$[CO_2] = C_{CO_2}^* (1 - e^{-k_L.a.(t-(t_1+t_2))}) \quad (41)$$

From the asymptotic model, the pH evolution can be predicted by:

Phase 1

$$pH = 14 + \log_{10}([OH^-]_0 - 2.E.k_L.a.C_{CO_2}^*.t) \quad t \in [0; t_1[\quad (42)$$

Phase 2

$$pH = -\log_{10}(K_{a2}) - \log_{10}\left(\frac{2.k_L.a.C_{CO_2}^*. (t - t_1)}{[CO_3^{2-}]_{t_1} - k_L.a.C_{CO_2}^*. (t - t_1)}\right) \quad t \in]t_1; t_1 + t_2[\quad (43)$$

$$pH = -\log_{10}(K_{a2}) - \log_{10}\left(\frac{2.k_L.a.C_{CO_2}^*. (t - t_1)}{[CO_3^{2-}]_{t_1} - k_L.a.C_{CO_2}^*. (t - t_1)}\right) \quad t \in]t_1; t_1 + t_2[\quad (44)$$

All parameters used in the asymptotic model are derived from time (0–250 s) and space averaged 1D complete model value and they are reported in Table 8. Fig. 9 reveals that the asymptotic model agrees well with 1D model results. The asymptotic model highlights that the essential parameters that control Phase 1 is related to E , k_L , and a . In Phase 2 and Phase 3, the most important parameters that control the pH evolution are just k_L and a . As CO_2 chemisorption rate is imposed by the mass transfer flux, it is actu-

Table 8
Parameters used in the asymptotic model.

Input Parameters	Value	Units
d_b	4.8	mm
ε_G	1.6	%
a	20	$m^2.m^{-3}$
u_G	0.289	$m.s^{-1}$
k_L	3×10^{-4}	$m.s^{-1}$
E	1.06	–
$C_{CO_2}^*$	0.0345	$kmol.m^{-3}$

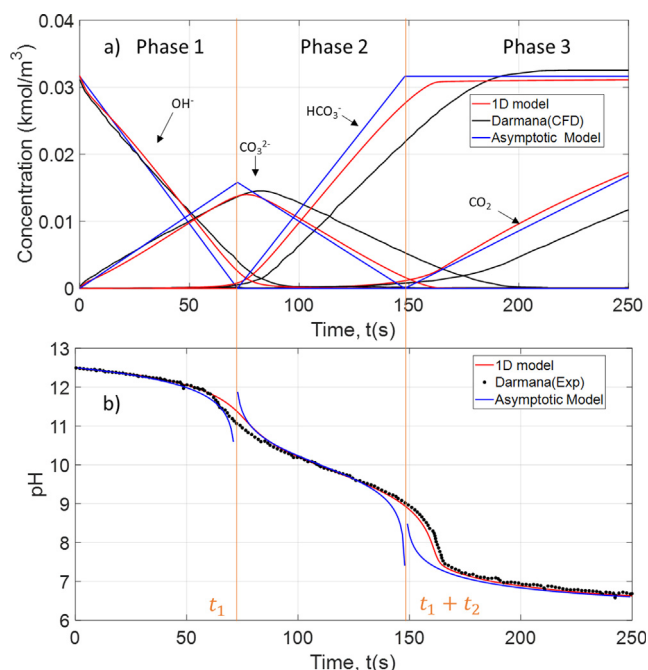


Fig. 9. (a) Temporal evolution of chemical species concentration with the asymptotic model described from equations (35)–(41) and (b) Time-dependent pH profile compared between (Darmana et al., 2007) CFD results, 1D model, asymptotic model (equations (42)–(44)).

ally not surprising to observe that the underlying mechanisms is totally controlled by mass transfer parameters, as proved by the asymptotic model and also discussed in the work of Huang et al. (2021). These parameters have to be modeled with utmost attention to give the most realistic prediction of temporal pH evolution. Sensitivity analyses on these parameters are thus carried out in Section 5.

Before sensitivity analysis, qualitative investigation can already be conducted with the asymptotic model, particularly from the expression of pH (equations (42)–(44)). The 0D model shows that the most impactful closure parameters in Phase 1 are E and k_L . From equation (42), it can be related that the higher the E , the higher the decrease in pH. Besides, it is proven through equation (37) that the higher the E , the shorter the t_1 , displacing the pH curve to the left.

On the contrary, Phase 2 is barely impacted by E , as shown in Fig. 7, whereby the non-enhanced mass transfer rate is nearly equal to the enhanced mass transfer rate. Nonetheless, it is still controlled by the k_L value as shown in equation (43). The slope of the pH curve is highly dependent of the mass transfer coefficient k_L . Phase 3 is analogous to Phase 2, having k_L as the determining parameter. In Phase 3, the only concentration evolution is that of $[CO_2]$, which changes according to the physical absorption flux.

The interfacial area a appears to be sensitive in every phase, signifying the importance of bubble diameter and gas holdup in the prediction of mass transfer flux. This also justifies the previous work using CFD approach for gas fraction calculation and bubble population model to better capture the mass transfer (Buffo et al., 2017; Krauß and Rzehak, 2018).

5. Discussions on sensitivity analyses using 1D model

With the good agreement of 1D and asymptotic model with experimental data, extensive sensitivity analyses have been conducted and they are compared with other researcher's work (Buffo et al., 2017; Hlawitschka et al., 2016; Huang et al., 2021; Krauß and Rzehak, 2018; Krauß and Rzehak, 2017; Liu et al., 2021). It is important to emphasize that the transient CO_2 chemisorption is measured by a pH probe located near the liquid free surface Darmana et al. (2007). This probe response integrates all the physical coupling (hydrodynamics, mass transfer and chemical reactions) taking place in the bubble column during the transient measurement, implying that the validation process is tricky, as several parameters have to be adjusted or predicted. The CFD approach is more complex compared to the 1D approach as it requires high computational resources to follow the overall chemical reaction spatially and temporally (plus integrating population balance model will further increase the simulation time). Regarding the complexity of the problem and long simulation time, it is difficult to validate a high-quality parametric study without extra consideration. For these aforementioned reasons, 1D model provides an interesting alternative for sensitivity analyses in view of short calculation time. Upon validation of hydrodynamics, inlet bubble diameter and reactive pathway in Section 3, the impact of other important parameters such as liquid mixing and mass transfer closure model are studied with the 1D model here. These sensitivity analyses also serve as a comprehensive comparison with the most recent CFD work as only certain results were compared and analyzed between them.

5.1. Influence of mixing

The liquid mixing in the 1D model is characterized by the axial dispersion coefficient D_L , in contrast to previous CFD work whereby the mixing in the bubble column is resolved.

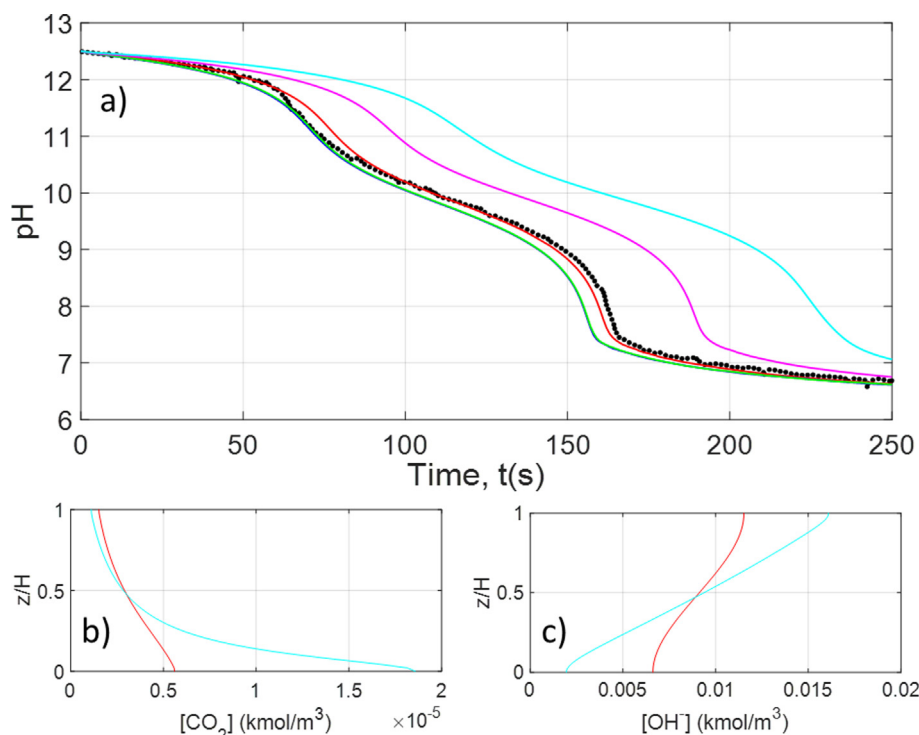


Fig. 10. (a) Time-dependent pH profile for different axial dispersion coefficient. Black dots from (Darmana et al., 2007) experimental results, Continuous lines from 1D model with Red lines $D_L = 5 \times 10^{-3} \text{ m}^2 \cdot \text{s}^{-1}$ (default value estimated from (Deckwer et al., 1974)), Cyan lines $D_L = 5 \times 10^{-5} \text{ m}^2 \cdot \text{s}^{-1}$, Magenta line $D_L = 5 \times 10^{-4} \text{ m}^2 \cdot \text{s}^{-1}$, Green line $D_L = 5 \times 10^{-2} \text{ m}^2 \cdot \text{s}^{-1}$, Blue line $D_L = 5 \times 10^{-1} \text{ m}^2 \cdot \text{s}^{-1}$. (b) Spatial profile of $[\text{CO}_2]$ at $t = 50$ s. (c) Spatial profile of $[\text{OH}^-]$ at $t = 50$ s. Red lines $D_L = 5 \times 10^{-3} \text{ m}^2 \cdot \text{s}^{-1}$. Cyan lines $D_L = 5 \times 10^{-5} \text{ m}^2 \cdot \text{s}^{-1}$.

Fig. 10a shows that D_L has an immediate impact in reproducing experimental pH curve with $5 \times 10^{-5} \text{ m}^2 \cdot \text{s}^{-1} < D_L < 5 \times 10^{-1} \text{ m}^2 \cdot \text{s}^{-1}$. The value of 5×10^{-5} is about one order of magnitude lower than the estimated turbulent diffusivity ($10^{-4} \text{ m}^2 \cdot \text{s}^{-1}$ as calculated in Section 2.2.1) and 5×10^{-1} is about two orders of magnitude higher than the spatial dispersion to illustrate the extreme case. Low axial dispersion coefficient will create spatial heterogeneities in terms of dissolved concentration, as evidenced in Fig. 10b & Fig. 10c. The lower the D_L , the greater the concentration difference between the top and the bottom of the column. As CO_2 is sparged at the bottom of the column, fast chemical reaction has already initiated at the lower half of the column, leaving less CO_2 at the top of the column to react with OH^- ions. Thus, with a low value of D_L , a moderate decline of pH is obtained, as evidenced in Fig. 10a. With a higher axial dispersion coefficient, dissolved CO_2 is homogenized in the column, it reaches the top with higher concentration at an earlier time, leading to an earlier decrease in pH in the similar manner. Nonetheless, the results become insensitive to D_L , for D_L higher than a magnitude of $10^{-3} \text{ m}^2 \cdot \text{s}^{-1}$. The two pH curves of $D_L = 5 \times 10^{-2} \text{ m}^2 \cdot \text{s}^{-1}$ (green line) and $D_L = 5 \times 10^{-1} \text{ m}^2 \cdot \text{s}^{-1}$ (blue line) superpose with each other, showing that at perfectly mixed liquid behavior, the pH description converge to the same shape. This is in line with the conclusion of Krauß and Rzehak (2017) work whereby they captured the pH evolution with a perfectly mixed 0D model. Here, it is found that the value estimated from Deckwer et al. (1974) yields a good pH prediction, without additional fitting on other parameters.

The gaseous side axial dispersion coefficient D_G does not yield much influence to the results (results not shown). As mentioned in Section 3.2, the bubbles diameter varies between 5.5 mm and 3.7 mm during the chemisorption process, with almost identical u_{rel} at this range of bubble size. Thus, the spatial dispersion is expected to be less intense, which is typically the case in homogeneous regime at low gas holdup. Besides, considering the CO_2

diffusivity in air is three order of magnitude higher than that in water, the axial Peclet number is expected to be higher in the gaseous phase ($\frac{u_G d_b}{D_{\text{CO}_2, G}} > \frac{u_L d_b}{D_{\text{CO}_2, L}}$), signifying less spatial dispersion.

5.2. Influence of enhancement factor

The enhancement factor E is defined as the ratio between mass transfer fluxes through the phase interface with and without reaction, based on the same concentration driving force (Westertep et al., 1998). The effect of E has been highlighted in the work of Hlawitschka et al. (2016) and Liu et al. (2021). Without implementing E in the model, the mass transfer is underestimated, leading to a wrong pH temporal evolution that lags behind the experimental pH curve. In this work, the two E models presented in Section 2.2.3 are studied.

Krauß and Rzehak (2017) applied a 0D model to solely investigate the chemical kinetics and enhancement factor. The authors stated that approximate or simplified expressions for the enhancement factor derived from simple conceptual models of mass transfer (film, penetration, and renewal models) that appear frequently in reaction engineering textbooks should be considered with care. They also showed that the E applied in the original work of Darmana is not suitable at small values of instantaneous enhancement factor E_i which even become less than one (violated the condition for equation (25)), leading to an underestimated value of E (see Fig. 8a of (Krauß and Rzehak, 2017)). We agreed to this finding as an underestimated mass transfer flux was obtained when the enhancement factor model used by Darmana was applied to our 1D model (results not shown). This could partly explain why Darmana yielded a slower decrease in pH in the initial stage, as shown in Fig. 11 (black lines compared to black dots).

Many researchers (Hlawitschka et al., 2016; Huang et al., 2021; Liu et al., 2021) used a simple enhancement factor proposed by

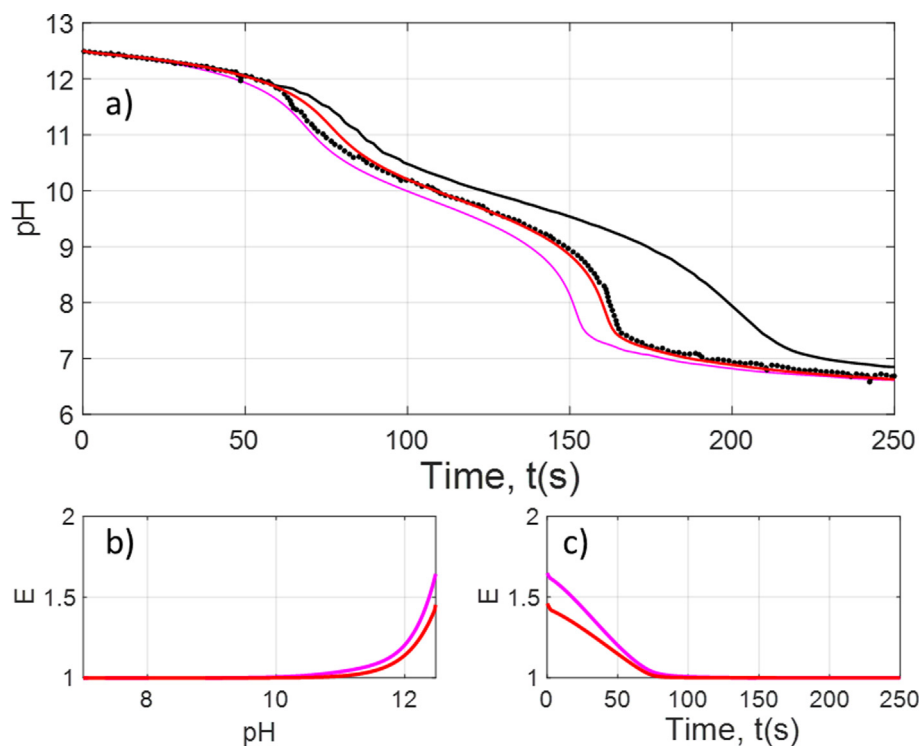


Fig. 11. (a) Time-dependent pH profile. Red lines with E from (Krauß and Rzehak, 2017), and Magenta lines with E from (Fleischer et al., 1996) (b) E vs pH and (c) Time-dependent E value.

Fleischer et al. (1996) which is derived from experimental data to reproduce Darmana's case. Krauß and Rzehak (2017) did not included this enhancement factor model in their comparison study. To the authors knowledge, the fit formula for the enhancement factor model proposed by Krauß and Rzehak (2017), has only been used in Krauß and Rzehak (2018) in the attempt to reproduce Darmana's case. Here, we compare the effectiveness between these two enhancement models of Fleischer et al. (1996) and Krauß and Rzehak (2017).

Fig. 11a depicts the pH curve obtained from two different enhancement models. The enhancement factor model proposed by Fleischer et al. (1996) is derived theoretically via two-film model which supposed the bubble interface is flat. The flat interface assumption is unrealistic unless the radius of the interface curvature is infinitely large. This leads to an overoptimistic value of E , which is reflected in Fig. 11b and Fig. 11c, as the initial drop of pH (magenta line) is the strongest for Fleischer et al. (1996).

The enhancement factor proposed by (Krauß and Rzehak, 2017) yields a slightly better description of the pH evolution at the beginning which extend to the overall pH curve. Nevertheless, the difference remains significantly small for these two models. This parameter should not be the determining factor to capture the overall pH curve, as it equals to 1 after 75 s.

It is also preferable to apply an analytical model such as that of Krauß and Rzehak (2017) rather than empirical correlation to perform any predictive simulation. To conclude this subsection, it is clear that E is impactful to the pH prediction as early as the process starts. Therefore, it changes t_1 , which causes a translation of the remaining pH curve. This has been initially proven by the asymptotic model as the parameter E appears only in the governing equation in Phase 1 (see equation (42)).

5.3. Influence of Sherwood number

Study of different mass transfer coefficient has been done in the recent work of (Huang et al., 2021; Liu et al., 2021) and it is also

implemented here for the sensitivity analysis. Another mass transfer model tested is that proposed by Higbie (1935), which is often applicable for clean spherical bubbles over 2 mm (Cockx et al., 1999; Fayolle et al., 2007; Larsson et al., 2022; Solsvik, 2018). These mass transfer models are summarized in Table 9.

Fig. 12 demonstrates the importance of Sherwood closure model on the CO_2 mass transfer flux. These Sherwood closure models are developed for different bubble geometrical characteristic under different hydrodynamics and physicochemical conditions (see Table 9). The k_L derived by Brauer (1979) is found to be the most suitable model. It is also used by Darmana et al. (2007) in their simulation. It is derived for non-spherical bubbles in the wobbling regime – this is typically the case for the bubbles having a size of 5.5 mm as it considers the stochastic deformation of the interface induced by turbulent motion in the surrounding fluid (Clift et al., 1978; Tomiyama et al., 1998). Thus, it offers a higher mass transfer coefficient than $k_{L,2}$, leading to a much higher CO_2 interfacial mass transfer flux, hence, a larger drop in terms of pH. To our knowledge, the classical mass transfer model of Higbie $k_{L,3}$ has not been applied in earlier CFD work of this context. Fig. 12 shows that the mass transfer model proposed by Higbie (1935) overestimates the mass transfer flux, leading to a faster drop in pH than the experimental pH curve.

Table 9
Mass transfer models derived from different Sherwood correlations.

Sherwood correlation	Notation	Description	Reference
$Sh = 2 + 0.015Re^{0.89}.Sc^{0.7}$	$k_{L,1}$	Non-spherical bubbles with stochastic deformations of the interface	(Brauer, 1979)
$Sh = 2 + 0.6415Re^{0.5}.Sc^{0.5}$	$k_{L,2}$	Spherical bubbles	(Bird et al., 2002)
$Sh = 1.13Re^{0.5}.Sc^{0.5}$	$k_{L,3}$	Clean spherical bubbles	(Higbie, 1935)

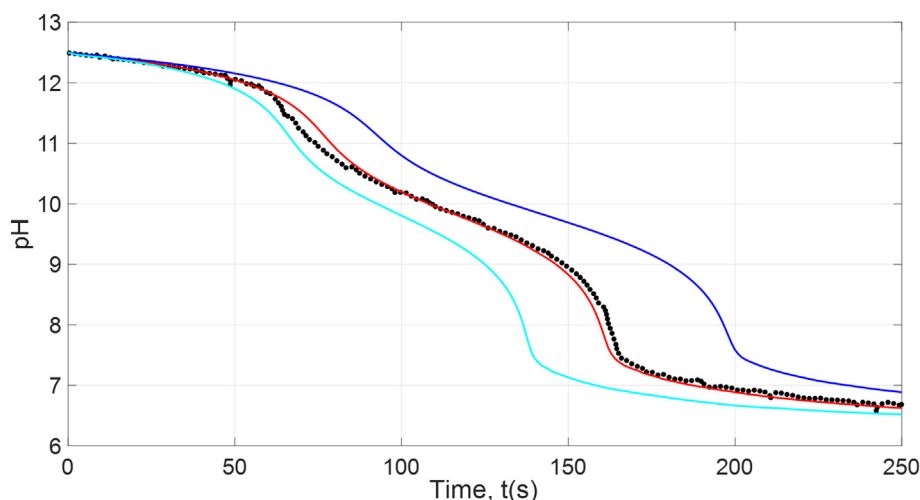


Fig. 12. Time-dependent pH profile using different k_L closure models. Black dots from (Darmana et al., 2007) experimental results, Colored lines from 1D model. Cyan lines from $k_{L,3}$, Red lines from $k_{L,1}$, and Blue lines from $k_{L,2}$.

Considering the Sherwood equation of Bird et al. (2002) and Higbie (1935), both have the classical exponent value of 0.5 for the Reynolds and Schmidt number, which is derived from the penetration model of mass transfer. The difference between the two equations is the factor before Re and Sc , with 0.6415 ($= \sqrt{\frac{4}{3\pi}}$) and 1.13 ($= \sqrt{\frac{4}{\pi}}$), respectively. The Sherwood number calculated from Bird et al. (2002) is developed for a spherical gas bubble surrounded by a liquid in creeping flow regime ($Re \ll 1$). For Sherwood number of Higbie (1935), the bubble is rising in liquids free of surface-acting agent and it undergoes a constant toroidal circulation (Rybczynski-Hadamard circulation). It is found that Sherwood model of Bird et al. (2002) underestimates the mass transfer rate, probably due to the Re is not in the applicable range.

Moreover, it is found that Re of the bubble is in the range of 1000–1600 for all studies. In this range of Re , these Sherwood correlations yield the mass transfer coefficient which ranks from the highest to the lowest as follows: $k_{L,3} > k_{L,1} > k_{L,2}$. This ranking is reflected in the pH curve whereby the highest Sherwood leads to an earlier decrease in pH. In terms of the ranking between $k_{L,1}$, $k_{L,2}$ and $k_{L,3}$. The choice of k_L remains a major factor in the pH prediction as it influences the rate of change of pH, right from the start to the end of the reactive process. The most suitable k_L is that applicable for non-spherical wobbling bubbles of Brauer (1979) in the configuration of the bubble plume of Darmana with large ellipsoidal bubbles.

6. Conclusion

In this work, a two-way coupled spatio-temporal 1D model is applied to study CO_2 reactive absorption process in a bubble column, previously presented in the Darmana et al. (2007). It is found that 1D model performs just as well as previous studies performed with CFD model. The objective of this paper is not to combine all the improvements reported in the literature and to perform an updated CFD simulation of Darmana's case. In the contrary, it aims to integrate different strategies proposed from published works and compare with their results using the 1D model, like a novel insight of Darmana et al. (2007) case. Moreover, 1D model leads to an asymptotic 0D model that helps to capture the essential feature of reactive bubbly flow and to identify the underlying physical-chemical parameters which control these flows. Contrary to CFD simulation, 1D model yields fast results which is useful for

probing a wide range of physical parameters and conducting series of sensitivity analysis. After identifying such specific parameters, advanced CFD model can be used to study the impact of these parameters on the local field structure and the phase interaction in more details without hypothesis on the flow. In CO_2 -NaOH chemisorption case, the particular parameters to focus on in CFD are mass transfer coefficient k_L and inlet bubble diameter d_{b0} . The closure model applied to these two parameters must be given the utmost importance to successfully capture the interfacial mass transfer flux, and eventually the temporal pH curve. Several conclusions can be drawn from this work:

Gas phase hydrodynamics has to be closely modelled to give realistic mass transfer flux. In this work, it is well captured with a drift-flux loop model with a C_0 coefficient of 1.27 and an averaged liquid recirculation velocity of 4.2 cm.s^{-1} .

- Bubble size shrinkage due to CO_2 chemisorption is observed experimentally and it has to be well-characterized in order to yield a satisfactory pH prediction.
- A correct inlet bubble diameter d_{b0} is essential as it decides the bubble diameter evolution. It is shown that a good description of bubble size changes is important to determine the local mass transfer flux, as the value fluctuates in a factor of two between the top and the bottom of the column. The value of $d_{b0} = 5.5 \text{ mm}$ appears to be an accurate estimation, according to Darmana et al. (2007).
- The water pathway has to be considered to correctly describe the late stage of the neutralization process as proposed by Krauß and Rzehak (2017). An asymptotic model is proposed to describe the CO_2 reactive absorption process and to unravel the controlling parameters, such as E , k_L , and a .
- The axial dispersion coefficient of $5 \times 10^{-3} \text{ m}^2.\text{s}^{-1}$ calculated from the correlation of Deckwer et al. (1974) which is derived from circular bubble column is also reliable for pseudo-2D bubble column, as shown in the findings of Alexander and Shah (1976).
- The enhancement factor has a huge impact on the pH evolution only when $pH > 10$. The enhancement factor proposed by Krauß and Rzehak (2017) has a better edge over that of Fleischer et al. (1996).
- The Sherwood correlation of Brauer (1979) seems to be the appropriate model. It corresponds well for non-spherical bubbles as the bubble with a size of 5.5 mm is typically situated in the wobbling regime. In this wobbling regime, the continuous

bubble oscillation motion contributes to a higher mass transfer coefficient as found in this work too.

Finally, it is shown that only by applying a suitable combination of closure models and chemical kinetics (d_{b0} , C_0 , $u_{L,recirc}$, u_{dfloop} , D_L , E , k_L , reaction pathways), the experimental data can be reproduced perfectly by the two-way coupled spatio-temporal 1D model. In this work, it is found that the combination of enhancement factor from Krauß and Rzehak (2017), 3 reactions pathway as proposed by Krauß and Rzehak (2017), Sherwood correlation from Brauer (1979), d_{b0} of 5.5 mm and D_L correlation estimated from Deckwer et al. (1974) gives the closest results to that of Darmana et al. (2007) experimental data.

CRediT authorship contribution statement

Vincent Ngu: Methodology, Conceptualization, Writing – original draft, Software, Data curation, Validation. **Jérôme Morchain:** Supervision, Methodology, Conceptualization, Writing – review & editing. **Arnaud Cockx:** Supervision, Methodology, Conceptualization, Writing – review & editing.

Data availability

Data will be made available on request.

Declaration of Competing Interest

The authors declare that they have no known competing financial interests or personal relationships that could have appeared to influence the work reported in this paper.

Acknowledgement

The authors wish to thank Prof. Alain Liné for providing insightful comments to the manuscript.

Appendix A. Solubility

The solubility of CO₂ in water $C_{CO_2}^*$ is described by a Henry constant which can take several forms (Sander, 2015). For this work, the dimensionless ratio (H) of the concentration in the liquid phase to the equilibrium concentration at the gas phase is used. The correlation for the temperature dependence dimensionless Henry constant for CO₂ in pure water ($He_{CO_2}^w$) proposed by Versteeg and Van Swaaij (1988) was used. This correlation was also applied in Huang et al. (2021) and Krauß and Rzehak (2018).

$$He_{CO_2}^w = 3.54 \cdot 10^{-7} RT \exp\left(\frac{2044}{T}\right) \quad (A.1)$$

Due to salting out effect in electrolyte solutions, the solubility of most gases decreases with salt concentration. Therefore, the solubility of CO₂ in alkaline solution can be estimated by that of Weisenberger and Schumpe (1996), expressed as.

$$He_{CO_2} = He_{CO_2}^w 10^{-\sum (h_i + h_G) C_i} \quad (A.2)$$

Table A1
Parameters for equation (A.2).

Liquid phase	h_i (m ³ .kmol ⁻¹)	Gas phase	$h_{G,0}$ (m ³ .kmol ⁻¹)	h_T (m ³ .kmol ⁻¹ .K ⁻¹)
Na ⁺	0.1143	CO ₂	-0.0172	-0.338.10 ⁻³
OH ⁻	0.0839			
HCO ₃ ⁻	0.0967			
CO ₃ ²⁻	0.1423			

Where C_i is species concentration in kmol.m⁻³, $h_G = h_{G,0} + h_T \cdot (T - 298.15)$ and the corresponding constants h_i summarized in Table A.1.

Krauß and Rzehak (2017) pointed out that the use of equation (A.2) leads to a maximum decrease of 1.5 % in CO₂ solubility compared with its solubility in pure water for the case of Darmana et al. (2007). Nevertheless, equation (A.2) is implemented in our model in order to have a full model without additional hypothesis. In the end, the solubility $C_{CO_2}^*$ is calculated using equation (A.3).

$$C_{CO_2}^* = He_{CO_2} C_{G,CO_2} \quad (A.3)$$

Appendix B. Diffusivity

Similar to solubility, the temperature dependence of CO₂ molecular diffusivity in water ($D_{CO_2}^w$) is calculated from the correlation of Versteeg and Van Swaaij (1988) as.

$$D_{CO_2}^w = 2.35 \cdot 10^{-6} \exp\left(-\frac{2199}{T}\right) \quad (B.1)$$

The molecular diffusivity of CO₂ in electrolytes can be calculated from Ratcliff and Holdcroft (1963) correlation as.

$$D_{CO_2} = D_{CO_2}^w \left(1 + 0.624 \sum b_i \cdot C_i\right) \quad (B.2)$$

The b_i constants are given in Table B.1.

The temperature dependent molecular diffusion coefficient of other chemical species (D_i) is determined by the power-law fits proposed by Zeebe (2011) and it is expressed as.

$$D_i = D_i^0 \cdot \left(\frac{T}{T_i^{ref}} - 1\right)^{\gamma^i} \quad (B.3)$$

With the values of D_i^0 , T_i^{ref} , and γ^i are given in Table B.2.

Again, Krauß and Rzehak (2017) concluded that the decrease of CO₂ diffusivity due to ionic effect in Darmana et al. (2007) case is less than 0.5 %, considering negligible.

Table B1
Parameters for equation (B.2).

Species	b_i (m ³ .kmol ⁻¹)
Na ⁺	-0.0857
OH ⁻	-0.1088
HCO ₃ ⁻	-0.1150
CO ₃ ²⁻	-0.2450

Table B2
Parameters for equation (B.3).

Ion	$D_i^0 \cdot 10^9$ (m ² .s ⁻¹)	T_i^{ref} (K)	γ^i
Na ⁺	5.391	209.7	1.619
OH ⁻	26.65	216.5	1.658
HCO ₃ ⁻	7.016	204.0	2.394
CO ₃ ²⁻	5.447	210.3	2.193

Appendix C. Reaction rate constants

The reaction rate constants mostly follow the work presented by Krauß and Rzehak (2017). It is recalled here to a certain extent necessary for the model.

First reaction

The rate constant for the first forward reaction (equation (12)) is calculated by the correlation proposed by Pohorecki and Moniuk (1988), which is a function of ionic strength as follow.

$$k_{1,1} = k_{1,1}^{\infty} \cdot 10^{0.221I - 0.016I^2} \quad (C.1.1)$$

Where $k_{1,1}^{\infty}$ is the temperature dependence first forward rate constant at infinite dilution of ions, given by.

$$k_{1,1}^{\infty} = 10^{11.895 - \frac{2382}{T}} \quad (C.1.2)$$

I Represents the ionic strength and it can be calculated as

$$I = \frac{1}{2} \left([Na^+] \cdot Z_{Na^+}^2 + [OH^-] \cdot Z_{OH^-}^2 + [HCO_3^-] \cdot Z_{HCO_3^-}^2 + [CO_3^{2-}] \cdot Z_{CO_3^{2-}}^2 \right) \quad (C.1.3)$$

Where Z represents the valency of the dissolved ions, with $Z_{Na^+} = 1$, $Z_{OH^-} = -1$, $Z_{HCO_3^-} = -1$ and $Z_{CO_3^{2-}} = -2$.

The first reaction (equation (12)) is coupled with the auto-dissociation of water. Thus, the backward reaction rate of the first reaction can be obtained through the ratio relation of the equilibrium constants. The backward reaction can therefore be expressed as.

$$k_{1,2} = \frac{K_W}{K_{eq}^3} k_{1,1} \quad (C.1.4)$$

where K_W is the equilibrium constant of the ionization of water and K_{eq}^3 is the equilibrium constant of the third reaction (equation (14)). Here, the temperature dependence K_W proposed by Tsionopoulos et al. (1976) is used. The equilibrium constant K_{eq}^3 is calculated from a relation proposed by Edwards et al. (1978).

$$K_W = [H^+][OH^-] = 10^{\frac{-5840}{T} - 61.2062 - 22.48 \log_{10}(T)} \quad (C.1.5)$$

$$K_{eq}^3 = \frac{[HCO_3^-][H^+]}{[CO_2]} = \exp \left(-\frac{12090}{T} + 235.5 - 36.78 \ln(T) \right) \quad (C.1.6)$$

Second reaction

The second reaction involves a proton transfer, implying that the rate of reactions is very rapid (Eigen, 1954). The forward reaction of the second reaction equation (13) $k_{2,1}$ is in the order of 10^{10} – 10^{11} m³.kmol⁻¹.s⁻¹. Nevertheless, as shown by Darmana et al. (2007) and Krauß and Rzehak (2018), a much smaller value can be used, as long as $k_{2,1} \gg k_{1,1}$. Krauß and Rzehak (2017) showed that with $k_{2,1}$ of 10^4 m³.kmol⁻¹.s⁻¹ there is negligible influence on the results. A value of $k_{2,1} = 10^4$ m³.kmol⁻¹.s⁻¹ is thus used in our study to allow numerical simulations to be performed at a larger time step.

The backward reaction $k_{2,2}$ is calculated with the equilibrium constant of the second reaction K_{eq}^2 , as proposed by Hikita et al. (1976).

$$K_{eq}^2 = \frac{k_{2,1}}{k_{2,2}} = K_{eq}^{2,\infty} \cdot 10^{\left(\frac{1.01 \sqrt{[Na^+]}}{1+1.27 \sqrt{[Na^+]}} + 0.125 [Na^+] \right)} \quad (C.2.1)$$

where $K_{eq}^{2,\infty}$ is the temperature dependent rate at infinite dilution of sodium ions.

$$K_{eq}^{2,\infty} = 10^{\frac{1568.94}{T} + 0.4134 - 0.00673 \cdot T} \quad (C.2.2)$$

The backward reaction is therefore calculated as.

$$k_{2,2} = \frac{k_{2,1}}{K_{eq}^2} \quad (C.2.3)$$

Third reaction

Since only uncharged molecules are involved in the third forward reaction (equation (14)), the forward reaction rate constant $k_{3,1}$ depends solely on the temperature and not ionic strength. It is determined by the equation proposed by Johnson (1982) as.

$$k_{3,1} = \exp \left(-\frac{6.19 \cdot 10^4}{T} + 1247 - 183 \ln(T) \right) \quad (C.3.1)$$

The third backward reaction rate constant $k_{3,2}$ can be calculated with the equilibrium constant K_{eq}^3 introduced previously in equation (C.1.6).

$$k_{3,2} = \frac{k_{3,1}}{K_{eq}^3} \quad (C.3.2)$$

Appendix D. Supplementary data

Supplementary data to this article can be found online at <https://doi.org/10.1016/j.ces.2022.117963>.

References

- Alexander, B.F., Shah, Y.T., 1976. Axial dispersion coefficients in bubble columns. *Chemical Engineering J.* 11, 153–156. [https://doi.org/10.1016/0300-9467\(76\)80021-4](https://doi.org/10.1016/0300-9467(76)80021-4).
- Bird, R.B., Stewart, W., Lightfoot, E.N., 2002. *Transport Phenomena*, Second. ed. John Wiley and Sons Ltd, Inc.
- Brauer, H., 1979. Particle/Fluid Transport Processes. *Prog. Chem. Eng.* 19, 61–99.
- Buffo, A., Vanni, M., Marchisio, D.L., 2017. Simulation of a reacting gas–liquid bubbly flow with CFD and PBM: Validation with experiments. *Appl. Math. Model.* 44, 43–60. <https://doi.org/10.1016/j.apm.2016.11.010>.
- Camarasa, E., Carvalho, E., Meleiro, L.A.C., Maciel Filho, R., Domingues, A., Wild, G., Poncin, S., Midoux, N., Bouillard, J., 2001. Development of a complete model for an air–lift reactor. *Chemical Engineering Science*, 16th International Conference on Chemical Reactor Engineering 56, 493–502. [10.1016/S0009-2509\(00\)00253-0](https://doi.org/10.1016/S0009-2509(00)00253-0).
- Camarasa, E., Vial, C., Poncin, S., Wild, G., Midoux, N., Bouillard, J., 1999. Influence of coalescence behaviour of the liquid and of gas sparging on hydrodynamics and bubble characteristics in a bubble column. *Chem. Eng. Process. Process Intensif.* 38, 329–344. [https://doi.org/10.1016/S0255-2701\(99\)00024-0](https://doi.org/10.1016/S0255-2701(99)00024-0).
- Chen, J., Brooks, C.S., 2021. Experiments and CFD simulation of mass transfer and hydrodynamics in a cylindrical bubble column. *Chem. Eng. Sci.* 234, <https://doi.org/10.1016/j.ces.2020.116435>.
- Chou, P.Y., 1945. ON VELOCITY CORRELATIONS AND THE SOLUTIONS OF THE EQUATIONS OF TURBULENT FLUCTUATION. *Q. Appl. Math.* 3, 38–54.
- Clift, R., Gurace, J.R., Weber, M.E., 1978. *Bubbles, drops, and particles*, 3. print. ed. Acad. Press, New York, NY.
- Cockx, A., Do-Quang, Z., Liné, A., Roustan, M., 1999. Use of computational fluid dynamics for simulating hydrodynamics and mass transfer in industrial ozonation towers. *Chem. Eng. Sci.* 54, 5085–5090. [https://doi.org/10.1016/S0009-2509\(99\)00239-0](https://doi.org/10.1016/S0009-2509(99)00239-0).
- Colombet, D., Cockx, A., Guiraud, P., Legendre, D., 2013. Experiments and modelling of a draft tube airlift reactor operated at high gas throughputs. *Chem. Eng. Sci.* 104, 32–43. <https://doi.org/10.1016/j.ces.2013.08.044>.
- Danckwerts, P.V., Lannus, A., 1970. Gas–Liquid Reactions. *J. Electrochem. Soc.* 117, 369C. <https://doi.org/10.1149/1.2407312>.
- Darmana, D., Henket, R.L.B., Deen, N.G., Kuipers, J.A.M., 2007. Detailed modelling of hydrodynamics, mass transfer and chemical reactions in a bubble column using a discrete bubble model: Chemisorption of CO₂ into NaOH solution, numerical and experimental study. *Chem. Eng. Sci.* 62, 2556–2575. <https://doi.org/10.1016/j.ces.2007.01.065>.

- Deckwer, W.-D., Burckhart, R., Zoll, G., 1974. Mixing and mass transfer in tall bubble columns. *Chem. Eng. Sci.* 29, 2177–2188. [https://doi.org/10.1016/0009-2509\(74\)80025-4](https://doi.org/10.1016/0009-2509(74)80025-4).
- Deckwer, W.-D., Adler, I., Zaidi, A., 1978. A comprehensive study on co2-interphase mass transfer in vertical cocurrent and countercurrent gas-liquid flow. *The Canadian Journal of Chemical Engineering* 56, 43–55. <https://doi.org/10.1002/cjce.5450560107>.
- Deckwer, W.-D., Schumpe, A., 1993. Improved tools for bubble column reactor design and scale-up. *Chem. Eng. Sci.* 48, 889–911. [https://doi.org/10.1016/0009-2509\(93\)80328-N](https://doi.org/10.1016/0009-2509(93)80328-N).
- DeCoursey, W.J., 1974. Absorption with chemical reaction: development of a new relation for the Danckwerts model. *Chem. Eng. Sci.* 29, 1867–1872. [https://doi.org/10.1016/0009-2509\(74\)85003-7](https://doi.org/10.1016/0009-2509(74)85003-7).
- Edwards, T.J., Maurer, G., Newman, J., Prausnitz, J.M., 1978. Vapor-liquid equilibria in multicomponent aqueous solutions of volatile weak electrolytes. *AIChE J.* 24, 966–976. <https://doi.org/10.1002/aic.690240605>.
- Eigen, M., 1954. Methods for investigation of ionic reactions in aqueous solutions with half-times as short as 10–9 sec. Application to neutralization and hydrolysis reactions. *Discuss. Faraday Soc.* 17, 194–205. <https://doi.org/10.1039/DF9541700194>.
- Ertekin, E., Kavanagh, J.M., Fletcher, D.F., McClure, D.D., 2021. Validation studies to assist in the development of scale and system independent CFD models for industrial bubble columns. *Chem. Eng. Res. Des.* 171, 1–12. <https://doi.org/10.1016/j.cherd.2021.04.023>.
- Fayolle, Y., Cockx, A., Gillot, S., Roustan, M., Héduit, A., 2007. Oxygen transfer prediction in aeration tanks using CFD. *Chemical Engineering Science*, 8th International Conference on Gas-Liquid and Gas-Liquid-Solid Reactor Engineering 62, 7163–7171. <https://doi.org/10.1016/j.ces.2007.08.082>.
- Fleischer, C., Becker, S., Eigenberger, G., 1996. Detailed modeling of the chemisorption of CO2 into NaOH in a bubble column. *Chemical Engineering Science*, Chemical Reaction Engineering: From Fundamentals to Commercial Plants and Products 51, 1715–1724. [https://doi.org/10.1016/0009-2509\(96\)00030-9](https://doi.org/10.1016/0009-2509(96)00030-9).
- Gaddis, E.S., Vogelpohl, A., 1986. Bubble formation in quiescent liquids under constant flow conditions. *Chem. Eng. Sci.* 41, 97–105. [https://doi.org/10.1016/0009-2509\(86\)85202-2](https://doi.org/10.1016/0009-2509(86)85202-2).
- Gruber, M.C., Radl, S., Khinast, J.G., 2015. Rigorous modeling of CO2 absorption and chemisorption: The influence of bubble coalescence and breakage. *Chem. Eng. Sci.* 137, 188–204. <https://doi.org/10.1016/j.ces.2015.06.008>.
- Higbie, R., 1935. The Rate of Absorption of a Pure Gas into a Still Liquid during Short Periods of Exposure. *Trans. AIChE* 31, 365–389.
- Hikita, H., Asai, S., Takatsuka, T., 1976. Absorption of carbon dioxide into aqueous sodium hydroxide and sodium carbonate-bicarbonate solutions. *The Chemical Engineering Journal* 11, 131–141. [https://doi.org/10.1016/S0300-9467\(76\)80035-4](https://doi.org/10.1016/S0300-9467(76)80035-4).
- Hissnaga, A.M., Padoin, N., Paladino, E.E., 2020. Mass transfer modeling and simulation of a transient homogeneous bubbly flow in a bubble column. *Chem. Eng. Sci.* 218, <https://doi.org/10.1016/j.ces.2020.115531>.
- Hlawitschka, M.W., Kovács, P., Zähringer, K., Bart, H.-J., 2017. Simulation and experimental validation of reactive bubble column reactors. *Chemical Engineering Science*, 13th International Conference on Gas-Liquid and Gas-Liquid-Solid Reactor Engineering 170, 306–319. <https://doi.org/10.1016/j.ces.2016.12.053>.
- Hlawitschka, M.W., Drefenstedt, S., Bart, H.J., 2016. Local Analysis of CO2 Chemisorption in a Rectangular Bubble Column Using a Multiphase Euler-Euler CFD Code. *Journal of Chemical Engineering & Process Technology* 7, <https://doi.org/10.4172/2157-7048.1000300>.
- Hori, Y., Hayashi, K., Hosokawa, S., Tomiyama, A., 2017. Mass transfer from single carbon-dioxide bubbles in electrolyte aqueous solutions in vertical pipes. *Int. J. Heat Mass Transf.* 115, 663–671. <https://doi.org/10.1016/j.ijheatmasstransfer.2017.07.087>.
- Huang, Z., Yan, H., Liu, L., Gong, H., Zhou, P., 2021. Numerical modeling of reactive bubbly flows based on Euler-Lagrange approach. *Chem. Eng. Sci.* 239, <https://doi.org/10.1016/j.ces.2021.116640>.
- Johnson, K.S., 1982. Carbon dioxide hydration and dehydration kinetics in seawater. *Limnol. Oceanogr.* 27, 849–855. <https://doi.org/10.4319/lo.1982.27.5.0849>.
- Kantarci, N., Borak, F., Ülgen, K.O., 2005. Bubble column reactors. *Process Biochem.* 40, 2263–2283. <https://doi.org/10.1016/j.procbio.2004.10.004>.
- Kern, D.M., 1960. The hydration of carbon dioxide. *J. Chem. Educ.* 37, 14. <https://doi.org/10.1021/ed037p14>.
- Krauß, M., Rzehak, R., 2018. Reactive absorption of CO2 in NaOH: An Euler-Euler simulation study. *Chem. Eng. Sci.* 181, 199–214. <https://doi.org/10.1016/j.ces.2018.01.009>.
- Krauß, M., Rzehak, R., 2017. Reactive absorption of CO2 in NaOH: Detailed study of enhancement factor models. *Chem. Eng. Sci.* 166, 193–209. <https://doi.org/10.1016/j.ces.2017.03.029>.
- Larsson, T., Duran Quintero, C., Gillot, S., Cockx, A., Fayolle, Y., 2022. Development and validation of a comprehensive 1-D model to simulate gas hold-up and gas-liquid transfer in deep air-water bubble columns. *Chem. Eng. Sci.* 248, <https://doi.org/10.1016/j.ces.2021.117210>.
- Launder, B.E., Spalding, D.B., 1974. The numerical computation of turbulent flows. *Comput. Methods Appl. Mech. Eng.* 3, 269–289. [https://doi.org/10.1016/0045-7825\(74\)90029-2](https://doi.org/10.1016/0045-7825(74)90029-2).
- Liu, J., Zhou, P., Liu, L., Chen, S., Song, Y., Yan, H., 2021. CFD modeling of reactive absorption of CO2 in aqueous NaOH in a rectangular bubble column: Comparison of mass transfer and enhancement factor model. *Chem. Eng. Sci.* 230, <https://doi.org/10.1016/j.ces.2020.116218>.
- McCann, D.J., Prince, R.G.H., 1971. Regimes of bubbling at a submerged orifice. *Chem. Eng. Sci.* 26, 1505–1512. [https://doi.org/10.1016/0009-2509\(71\)86042-6](https://doi.org/10.1016/0009-2509(71)86042-6).
- McClure, D.D., Norris, H., Kavanagh, J.M., Fletcher, D.F., Barton, G.W., 2014. Validation of a Computationally Efficient Computational Fluid Dynamics (CFD) Model for Industrial Bubble Column Bioreactors. *Ind. Eng. Chem. Res.* 53, 14526–14543. <https://doi.org/10.1021/ie501105m>.
- McClure, D.D., Wang, C., Kavanagh, J.M., Fletcher, D.F., Barton, G.W., 2016. Experimental investigation into the impact of sparger design on bubble columns at high superficial velocities. *Chem. Eng. Res. Des.* 106, 205–213. <https://doi.org/10.1016/j.cherd.2015.12.027>.
- Ngu, V., Morchain, J., Cockx, A., 2022. Spatio-temporal 1D gas-liquid model for biological methanation in lab scale and industrial bubble column. *Chem. Eng. Sci.* 117478. <https://doi.org/10.1016/j.ces.2022.117478>.
- Pohorecki, R., Moniuk, W., 1988. Kinetics of reaction between carbon dioxide and hydroxyl ions in aqueous electrolyte solutions. *Chem. Eng. Sci.* 43, 1677–1684. [https://doi.org/10.1016/0009-2509\(88\)85159-5](https://doi.org/10.1016/0009-2509(88)85159-5).
- Ratcliff, G.A., Holdcroft, J.G., 1963. Diffusivities of gases in aqueous electrolyte solutions. *Trans. Inst. Chem. Eng.* 41, 315–319.
- Rehman, U., Audenaert, W., Amerlinck, Y., Maere, T., Arnaldos, M., Nopens, I., 2017. How well-mixed is well mixed? Hydrodynamic-biokinetic model integration in an aerated tank of a full-scale water resource recovery facility. *Water Sci. Technol.* 76, 1950–1965. <https://doi.org/10.2166/wst.2017.330>.
- Rzehak, R., Ziegenhein, T., Kriebitzsch, S., Krepper, E., Lucas, D., 2017. Unified modeling of bubbly flows in pipes, bubble columns, and airlift columns. *Chemical Engineering Science*, 12th International Conference on Gas-Liquid and Gas-Liquid-Solid Reactor Engineering 157, 147–158. <https://doi.org/10.1016/j.ces.2016.04.056>.
- Rzehak, R., Krepper, E., 2016. Euler-Euler simulation of mass-transfer in bubbly flows. *Chem. Eng. Sci.* 155, 459–468. <https://doi.org/10.1016/j.ces.2016.08.036>.
- Saito, T., Torii, M., 2015. Effects of a bubble and the surrounding liquid motions on the instantaneous mass transfer across the gas-liquid interface. *Chem. Eng. J.* 265, 164–175. <https://doi.org/10.1016/j.cej.2014.12.039>.
- Sander, R., 2015. Compilation of Henry's law constants (version 4.0) for water as solvent. *Atmos. Chem. Phys.* 15, 4399–4981. <https://doi.org/10.5194/acp-15-4399-2015>.
- Schäfer, R., Merten, C., Eigenberger, G., 2002. Bubble size distributions in a bubble column reactor under industrial conditions. *Exp. Therm Fluid Sci.* 26, 595–604. [https://doi.org/10.1016/S0894-1777\(02\)00189-9](https://doi.org/10.1016/S0894-1777(02)00189-9).
- Shah, Y.T., Kelkar, B.G., Godbole, S.P., Deckwer, W.-D., 1982. Design parameters estimations for bubble column reactors. *AIChE J.* 28, 353–379. <https://doi.org/10.1002/aic.690280302>.
- Siebler, F., Lapin, A., Takors, R., 2020. Synergistically applying 1-D modeling and CFD for designing industrial scale bubble column syngas bioreactors. *Engineering in Life Sciences* 20, 239–251. <https://doi.org/10.1002/elsc.201900132>.
- Solsvik, J., 2018. Lagrangian modeling of mass transfer from a single bubble rising in stagnant liquid. *Chem. Eng. Sci.* 190, 370–383. <https://doi.org/10.1016/j.ces.2018.06.002>.
- Taborda, M.A., Sommerfeld, M., 2021. Reactive LES-Euler/Lagrange modelling of bubble columns considering effects of bubble dynamics. *Chem. Eng. J.* 407, <https://doi.org/10.1016/j.cej.2020.127222>.
- Takemura, F., Yabe, A., 1999. Rising speed and dissolution rate of a carbon dioxide bubble in slightly contaminated water. *J. Fluid Mech.* 378, 319–334. <https://doi.org/10.1017/S0022112098003358>.
- Talvy, S., Cockx, A., Liné, A., 2007. Modeling hydrodynamics of gas-liquid airlift reactor. *AIChE J.* 53, 335–353. <https://doi.org/10.1002/aic.11078>.
- Talvy, S., Cockx, A., Liné, A., 2005. Global modelling of a gas-liquid-solid airlift reactor. *Chemical Engineering Science*, 7th International Conference on Gas-Liquid and Gas-Liquid-Solid Reactor Engineering 60, 5991–6003. <https://doi.org/10.1016/j.ces.2005.04.067>.
- Tanaka, S., Kastens, S., Fujioka, S., Schlüter, M., Terasaka, K., 2020. Mass transfer from freely rising microbubbles in aqueous solutions of surfactant or salt. *Chem. Eng. J.* 387, <https://doi.org/10.1016/j.cej.2019.03.122>.
- Tiruneh, G., Norddahl, B., 2016. The influence of polymeric membrane gas spargers on hydrodynamics and mass transfer in bubble column bioreactors. *Bioprocess Biosyst. Eng.* 39, 613–626. <https://doi.org/10.1007/s00449-016-1543-7>.
- Tomiyama, A., Matsuoka, T., Fukuda, T., Sakaguchi, T., 1995. A Simple Numerical Method for Solving an Incompressible Two-Fluid Model in a General Curvilinear Coordinate System, in: Serizawa, A., Fukano, T., Bataille, J. (Eds.), *Multiphase Flow 1995*. Elsevier, Amsterdam, pp. 241–252. <https://doi.org/10.1016/B978-0-444-81811-9.50026-3>.
- Tomiyama, A., Kataoka, I., Zun, I., Sakaguchi, T., 1998. Drag Coefficients of Single Bubbles under Normal and Micro Gravity Conditions. *JSME International Journal Series B* 41, 472–479. <https://doi.org/10.1299/jsmeb.41.472>.
- Tomiyama, A., Tamai, H., Zun, I., Hosokawa, S., 2002. Transverse migration of single bubbles in simple shear flows. *Chem. Eng. Sci.* 57, 1849–1858. [https://doi.org/10.1016/S0009-2509\(02\)00085-4](https://doi.org/10.1016/S0009-2509(02)00085-4).
- Tsonopoulos, C., Coulson, D.M., Inman, L.B., 1976. Ionization constants of water pollutants. *J. Chem. Eng. Data* 21, 190–193. <https://doi.org/10.1021/je60069a008>.
- Versteeg, G.F., Van Swaaij, W.P.M., 1988. Solubility and diffusivity of acid gases (carbon dioxide, nitrous oxide) in aqueous alkaline solutions. *J. Chem. Eng. Data* 33, 29–34. <https://doi.org/10.1021/je00051a011>.
- Wachi, S., Nojima, Y., 1990. Gas-phase dispersion in bubble columns. *Chem. Eng. Sci.* 45, 901–905. [https://doi.org/10.1016/0009-2509\(90\)85012-3](https://doi.org/10.1016/0009-2509(90)85012-3).

- Weisenberger, S., Schumpe, A., 1996. Estimation of gas solubilities in salt solutions at temperatures from 273 K to 363 K. *AIChE J.* 42, 298–300. <https://doi.org/10.1002/aic.690420130>.
- Westerterp, A., Swaaij, K.R., Beenackers, W.P.M., 1998. *Chemical Reactor Design and Operation*. New York.
- Zeebe, R.E., 2011. On the molecular diffusion coefficients of dissolved CO₂, HCO₃⁻, and CO₃²⁻ and their dependence on isotopic mass. *Geochim. Cosmochim. Acta* 75, 2483–2498. <https://doi.org/10.1016/j.gca.2011.02.010>.
- Zuber, N., Findlay, J.A., 1965. Average Volumetric Concentration in Two-Phase Flow Systems. *J. Heat Transfer* 87, 453–468. <https://doi.org/10.1115/1.3689137>.